Nanoscale

ROYAL SOCIETY OF CHEMISTRY

PAPER

View Article Online
View Journal | View Issue

Cite this: *Nanoscale*, 2024, **16**, 17024

A comparative study on surface-engineered nanoceria using a catechol copolymer design: colloidal stability *vs.* antioxidant activity†

Milad Ghorbani,[a,b] Francesca Ercole,[a] Katayoun Nazemi,[a] Nicole M. Warne,[a] John F. Quinn *[a,c] and Kristian Kempe *[a,b]

Received 28th May 2024,
Accepted 13th August 2024

DOI: 10.1039/d4nr02247e

rsc.li/nanoscale

Nanoceria (NC) are widely studied as potent nanozyme antioxidants, featuring unique multifunctional, self-regenerative, and high-throughput enzymatic functions. However, bare NC are reported to show poor colloidal stability in biological media. Despite this, the nexus between colloidal stability and antioxidant activity has rarely been assessed. Here, a library of three copolymeric stabilising agents was synthesised, each consisting of hydrophilic poly(oligo(ethylene glycol) methyl ether methacrylate) brushes (P(OEGMA)) and a novel catechol anchoring block, and used for surface engineering of NC. The colloidal stability of the surface-engineered NC was assessed in phosphate buffered saline (PBS) by monitoring their precipitation *via* UV-Vis spectrophotometry, and their catalase (CAT)- and superoxide dismutase (SOD)-like activities were analysed using fluorospectrophotometry. The obtained results indicate that P(OEGMA) coating improves colloidal stability of NC over 48 h, highlighting the stable attachment of catechol functionalities to the surface of NC. In addition, X-ray photoelectron spectroscopy (XPS) indicates that the catechol functionalities lead to an increase in Ce^{3+}/Ce^{4+} ratio and the concentration of oxygen vacancies, depending on the number of catechol units. Altogether, surface engineering of NC optimally results in an increase in CAT- and SOD-like activities by, respectively, 41% (=57.7% H_2O_2 elimination) and 78% (=78.0% $O_2^{\bullet-}$ elimination) relative to bare NC, signifying a positive correlation between colloidal stability and antioxidant activity of the NC nanozymes.

1. Introduction

Nanozyme antioxidants have emerged as powerful antioxidants over the last decades for the treatment of, for example Parkinson's disease, Alzheimer's disease, transient ischemic attacks, amyotrophic lateral sclerosis, and stroke by mitigating oxidative stress and inflammation.[1,2] For example, in a recent study, Ma *et al.* investigated the antioxidant activity of nanobiominerals and reported a potent superoxide-diminishing activity for the iron core of prokaryote ferritin, depending on the iron/phosphate ratio changes in the iron core, that enhanced resistance to superoxide in *E. coli*.[3]

Cerium oxide (CeO_2) nanoparticles (nanoceria, NC) have been introduced as promising nanozyme antioxidants owing to their unique self-regenerative redox function, multifunctional and strong antioxidant activity, ample specific surface area, biocompatibility, highly tuneable surface chemistry, and enzymatic stability over a wide range of pH and temperature.[4,5] Nanoceria have been reported to strongly neutralise various kinds of free radicals at neutral/physiological pH *via* superoxide dismutase (SOD)-like[6] and catalase (CAT)-like activities,[7] as well as hydroxyl[8] and nitric oxide[9] radical-scavenging activities. Of these, the SOD- and CAT-like activities of NC have been more extensively scrutinised and reported.[5] Specifically, the redox couple of Ce^{3+}/Ce^{4+} and oxygen vacancies, that account for highly reactive defect sites, are thought to play vital roles in the catalytic activity of NC.[10] For SOD-like activity,[11] the reaction is initiated by $O_2^{\bullet-}$ radicals binding with oxygen vacancies available around Ce^{3+} in the crystal lattice of NC. Thereafter, electron transfer from Ce^{3+} to an oxygen atom and binding of two H^+ with two oxygen atoms yields H_2O_2, which then oxidises Ce^{3+} to Ce^{4+}. The generated H_2O_2 can also reduce Ce^{4+} back to Ce^{3+}, thus providing a means for a continuous, long-

[a]*Drug Delivery, Disposition and Dynamics, Monash Institute of Pharmaceutical Sciences, Monash University, Parkville, Victoria 3052, Australia. E-mail: john.f.quinn@monash.edu*
[b]*Materials Science and Engineering, Monash University, Clayton, Victoria 3800, Australia. E-mail: kristian.kempe@monash.edu*
[c]*Department of Chemical and Biological Engineering, Faculty of Engineering, Monash University, Clayton, Victoria 3800, Australia*

†Electronic supplementary information (ESI) available: Literature review summary (Fig. S1 and Table S1) as well as ^{1}H NMR (Fig. S2–S15 and Table S3), SEC (Fig. S16–S18 and Tables S2–S3), TEM (Fig. S20), XPS (Fig. S21), colloidal stability (Fig. S22–S24), and cytotoxicity (Fig. S25) analyses results. See DOI: https://doi.org/10.1039/d4nr02247e

lasting catalytic activity and the so-called self-regenerative property of NC. For CAT-like activity,[11] NC contributes to neutralising H_2O_2 in two steps. Firstly, one H_2O_2 molecule associates with NC, reducing Ce^{4+} to Ce^{3+}, with release of H^+ and O_2. Secondly, a further H_2O_2 molecule interacts with an oxygen vacancy leading to formation of Ce^{4+} and subsequent release of a water molecule. Given the respective mechanisms, it has been reported that higher concentrations of Ce^{3+} in the NC favours SOD-like activity, while CAT-like activity is more pronounced for higher concentrations of Ce^{4+}.[12,13]

Significantly, as noted in a comprehensive review published in 2015, bare NC are colloidally unstable in biological and saline buffer media, with formation of large aggregates and thus precipitation of nanoparticles over time.[14] This would be expected to dramatically change the surface properties of NC and hence adversely affect their antioxidant activity due to (i) decreased specific surface area, (ii) reduced interactions with target substrates or cells, and (iii) potential impacts on Ce^{3+}/Ce^{4+} ratio and available oxygen vacancies.

To assess the state-of-the-art in relation to colloidal stability and antioxidant activity, we reviewed 100 studies describing the antioxidant properties of NC (out of 235; confidence interval 99%) published in Q1 journals (according to SCImago Journal & Country Rank) since 2016 using the Scopus database (keywords: nanoceria, cerium oxide, antioxidant). Colloidal stability analysis (Fig. S1a and Table S1†) was only included in 23 studies ($P < 0.0001$, chi-squared test, expected value for each group 50%), and 38 studies did not report the use of any stabilising agents. Additionally, pure water was used to investigate the colloidal stability in 11 of those 23 studies (Fig. S1b†). It is well-established that water lacks the crucial elements of saline buffer and cell culture media, *i.e.*, electrolytes and biomolecules, that are thought to impact the colloidal stability of nanoparticle dispersions.[15] Our literature survey also indicated that dynamic light scattering (DLS) was the most frequently used technique to assess colloidal stability. Despite the strengths of this method for analysing size distribution, DLS only detects those nanoparticles suspended in the supernatant and is therefore not informative about the amount of precipitated/deposited nanoparticles resulting from colloidal instability over time. Of the studied stabilising agents, synthetic hydrophilic polymers with linear structures, *i.e.*, poly(acrylic acid) (PAA) and poly(ethylene glycol) (PEG), are among the most frequently applied stabilising agents (Fig. S1c†). Hydrophilic polymers with more complex architectures that could potentially favour colloidal stability, *e.g.*, brush-type configurations, have rarely been used.[16] It is also worth noting that a potential correlation between colloidal stability and antioxidant activity of NC-based nanozymes was only observed in nine studies (Table S1†). Kwon *et al.*[17] stabilised NC with a PEG-based polymeric structure (DSPE-PEG-TPP) and observed an insignificant change in hydrodynamic size of the samples following one month in saline buffer, cell culture, and human blood plasma media. However, these authors reported a reduction in SOD- and CAT-like activities of DSPE-PEG-TPP stabilised NC, which may be attributed to the DSPE-PEG-TPP layer hampering access of $O_2^{\bullet-}$ and H_2O_2 molecules to the surface of NC. Mitra *et al.*[18] coated NC with a glycol chitosan polymer matrix (GCCNPs), leading to noticeable stability in water, as evidenced by no apparent sedimentation. In this case, the particles exhibited significantly improved antioxidant activity compared to bare NC. Nonetheless, the research did not investigate the relationship between colloidal stability and antioxidant stability. In addition, colloidal stability was measured by either DLS (which does not consider sedimentation over time) or merely by visual assessments, which may not provide reproducible results. Moreover, the effect of anchoring units on colloidal stability and, potentially, antioxidant activity of NC has not been discussed.

Herein, we investigated the colloidal stability of NC in saline buffer medium *via* a reproducible methodology yielding information about both dispersed and precipitated nanoparticles. In addition, we designed and synthesised a stabilising agent based on hydrophilic poly(oligo(ethylene glycol) methyl ether methacrylate) brush-type polymers (P(OEGMA)) to improve colloidal stability of NC in saline buffer medium. Finally, we assessed the CAT- and SOD-like activities of P(OEGMA)-stabilised NC and scrutinised the potential interplay between colloidal stability and antioxidant performance.

To this end, a novel anchoring agent with catechol functionality was first synthesised and then added as a block to a hydrophilic P(OEGMA) segment using reversible addition–fragmentation chain-transfer (RAFT) polymerisation. Using this methodology, a library of three block copolymer stabilising agents was synthesised, with variations in chain length for both the hydrophilic and anchoring blocks. This approach was applied to allow the impact of block copolymer composition on colloidal stability and antioxidant function of NC to be investigated. Bare NC were coated with the stabilising agents, and the colloidal stability of each system was investigated using a UV-Vis method in a phosphate buffered saline medium (PBS, 1×, pH 7.4). Additionally, the CAT- and SOD-like activities of the bare and copolymer-coated NC samples were analysed in acellular conditions *via* fluorescence spectroscopy. Overall, surface-engineered NC showed potent CAT-like (=57.7% H_2O_2 elimination) and SOD-like (=78.0% $O_2^{\bullet-}$ elimination) activities. Also, the results suggested that the stabilising agents could improve the colloidal stability of NC in PBS to an extent that exhibited a positive correlation with CAT- and SOD-like activities. Nevertheless, colloidal stability was found not to be the only relevant factor, as the antioxidant activity of NC is also potentially influenced by the grafting density of the stabilising agent, Ce^{3+}/Ce^{4+} ratio, the oxygen vacancy concentration, interactions of the anchoring block with the NC surface, as well as the identity of the reactive oxygen species (*i.e.*, $O_2^{\bullet-}$ *vs.* H_2O_2).

2. Experimental

2.1. Materials

Cerium(IV) oxide nanopowder (Nanoceria, <25 nm particle size (BET)), oligo(ethylene glycol) methyl ether methacrylate

($OEGMA_{500}$) (M_n = ~500 g mol^{-1}), azobisisobutyronitrile (AIBN), 1,1′-azobis(cyclohexanecarbonitrile) (ACHN), 4-cyano-2-propyl benzodithioate (CPBDT) (>97% HPLC), anhydrous triethylamine (TEA, ≥99%), anhydrous dichloromethane (DCM, ≥99%), isobutyl chloroformate, *N*-methyl morpholine, ethanolamine, methacrylic anhydride, isopropylamine (IPAM), phosphate buffered saline (PBS) tablets, hydrogen peroxide (H_2O_2, 50 wt% in H_2O), anhydrous dimethyl sulfoxide (DMSO), terephthalic acid (TA, 98%), xanthine (X), xanthine oxidase (XO), and Dulbecco's modified Eagle's medium-high glucose (DMEM) were purchased from Sigma-Aldrich. $OEGMA_{500}$ was passed through a column of basic alumina in order to remove inhibitor before use, and AIBN was purified by recrystallization from methanol before use. Hydrochloric acid (32%) and sodium bicarbonate were procured from Ajax Finechem. Fetal bovine serum (FBS) was acquired from ThermoFisher Scientific. Alamar Blue cell viability reagent was obtained from Invitrogen. Tetrahydrofuran (THF) was purchased from Merck Millipore (Burlington, MA, USA). Dihydroethidium (HE) was obtained from Aaron Chemicals LLC.

2.2. Characterisations

^1H (400 MHz) NMR spectra were acquired using a Bruker UltraShield 400 MHz spectrometer at 25 °C. Samples were dissolved in deuterated chloroform ($CDCl_3$) or deuterated dimethyl sulfoxide (DMSO-d_6) (Cambridge Isotope Labs), and chemical shifts were reported as parts per million from external tetramethylsilane. Size exclusion chromatography (SEC) was conducted using a Shimadzu modular system comprised of a DGU-12A degasser, an SIL-20 AD automatic injector, a 5.0 μm bead-size guard column (50 mm × 7.8 mm), three KF-805 L columns (300 mm × 8 mm, bead size: 10 μm, pore size maximum: 5000 A), an SPD-20A ultraviolet (UV) detector, and an RID-10A differential refractive index (RI) detector. A CTO-20A oven was employed to keep the temperature of the columns at 40 °C. *N*,*N*-Dimethylacetamide (DMAc, HPLC grade, 0.03% w/v LiBr) was used as the eluent, and the flow rate was maintained at 1 mL min^{-1} employing an LC-20 AD pump. Commercial PS standards with molecular weights ranging from 500 to 2 × 10^6 g mol^{-1} were applied to acquire the molecular weight calibration curve. Polymer solutions were filtered through 0.45 μm filters before injection, and number-average molecular weight (M_n, SEC) and dispersity ($Đ$) values were determined *via* Shimadzu LabSolutions software. Dynamic light scattering (DLS) and zeta potential measurements were carried out using a Malvern Zetasizer Nano ZS in Milli-Q water at 25 °C. Transmission Electron Microscopy (TEM) imaging was performed with an FEI Tecnai G2 T-20 microscope operating at 200 kV accelerating voltage from a lanthanum hexaboride (LaB_6) thermal emitter. TEM samples were prepared by pipetting 3 μL of a 1 mg mL^{-1} nanoparticle dispersion solution onto the surface of a plasma de-contaminated (XEI Scientific Evactron® 25, 10 seconds) carbon coated copper grid (ProSciTech). Excess solution was wicked away, before the grids were air dried. TEM images were captured *via* WA-Orius CCD camera, and nanoparticle size was measured by ImageJ 1.54f. UV–vis spectra were measured using a UV–vis spectrophotometer (Shimadzu UV-3600 UV–vis–near-infrared). Attenuated Total Reflection Fourier Transform Infrared spectroscopy (ATR-FTIR) was conducted using an IRTracer-100 Fourier Transform Infrared (FTIR) spectrophotometer provided with a He–Ne laser and an MCT (Hg–Cd–Te) detector under liquid nitrogen cooling. X-ray powder diffraction (XRD) patterns were captured using an X-ray diffractometer (Shimadzu XRD-7000) at 2Theta angle range of 20°–90°. X-ray photoelectron spectroscopy (XPS) was carried out using a Thermo Scientific Nexsa Surface Analysis System equipped with a hemispherical analyser. The incident radiation was monochromatic Al Kα X-rays (1486.6 eV) at 72 W (6 mA and 12 kV, 400 × 800 $μm^2$ spot). The general survey (wide) and high-resolution (narrow) scans were respectively recorded at analyser pass energies of 150 and 50 eV, and step sizes of 1.0 eV and 0.1 eV. The base pressure in the analysis chamber was less than 5.0 × 10^{-9} mbar. In order to compensate for surface charging, a low-energy dual-beam (ion and electron) flood gun was applied. Data analysis was performed *via* Avantage software v5.9931, where the energy calibration was referenced to the main line of C1s at 284.8 eV, and the Smart background was employed for curve fitting. Thermogravimetric Analysis (TGA) was conducted on a Pyris 1 TGA instrument (PerkinElmer) at the temperature range of 50–1000 °C and a 20 °C min^{-1} heating rate. Fluorescence spectroscopy analysis was conducted on a Shizmazdu RF-5301PC spectrofluorophotometer using a 500 μL quartz SUPRASIL cuvette.

2.3. Synthesis of iBoc-protected dihydrocaffeate methacrylate monomer (prCAT monomer)

Synthesis of prCAT monomer consisted of three steps as detailed below (Scheme 1):

2.3.1. Step (1) synthesis of 3-(3,4-bis((isobutoxycarbonyl)oxy)phenyl)propanoic (isobutyl carbonic) anhydride (iBoc-protected dihydrocaffeic acid carbonic anhydride, iBocDHCA). 3-(3,4-Dihydroxyphenyl)propanoic acid (dihydrocaffeic acid) (2.0 g, 11.0 × 10^{-3} mol) was introduced into an oven-dried round bottom flask followed by the addition of dry THF (50 mL) and isobutyl chloroformate (4.7 g, 4.4 mL, 34.0 × 10^{-3} mol). The solution was cooled using an ice/salt (−15 °C) bath and kept under nitrogen. To the stirring solution was added *N*-methyl morpholine (3.5 g, 3.9 mL, 35.0 × 10^{-3} mol) dropwise after which the solution was left stirring at ambient temperature for 1 h. Petroleum benzine 60–80 °C (20 mL) was then added to the reaction mixture, and the solids were filtered out. The filtrate was then evaporated, and the resulting crude oil was purified by silica gel flash chromatography using ethyl acetate (EtOAc)/petroleum benzine 60–80 °C (1 : 9 → 1 : 1 v/v) to afford the product, iBocDHCA, as a clear oil (3.1 g, 60% yield). ^1H NMR (400 MHz, $CDCl_3$) δ ppm: 7.21 (1H, d, J = 8.2 Hz, ArH), 7.14–7.10 (2H, m, ArH), 4.05 (2H, d, J = 6.6 Hz, CH_2, isobutyl), 4.03 (2H, d, J = 6.7 Hz, CH_2, isobutyl), 4.02 (2H, d, J = 6.6 Hz, CH_2, isobutyl), 3.00 (2H, t, J = 7.6 Hz, CH_2), 2.79 (2H, t, J = 7.6 Hz, CH_2), 2.09–1.98 (3H, m, CH, isobutyl), 1.01–0.96 (18H, m, 6 × CH_3, isobutyl). ^{13}C NMR (100 MHz, $CDCl_3$) δ

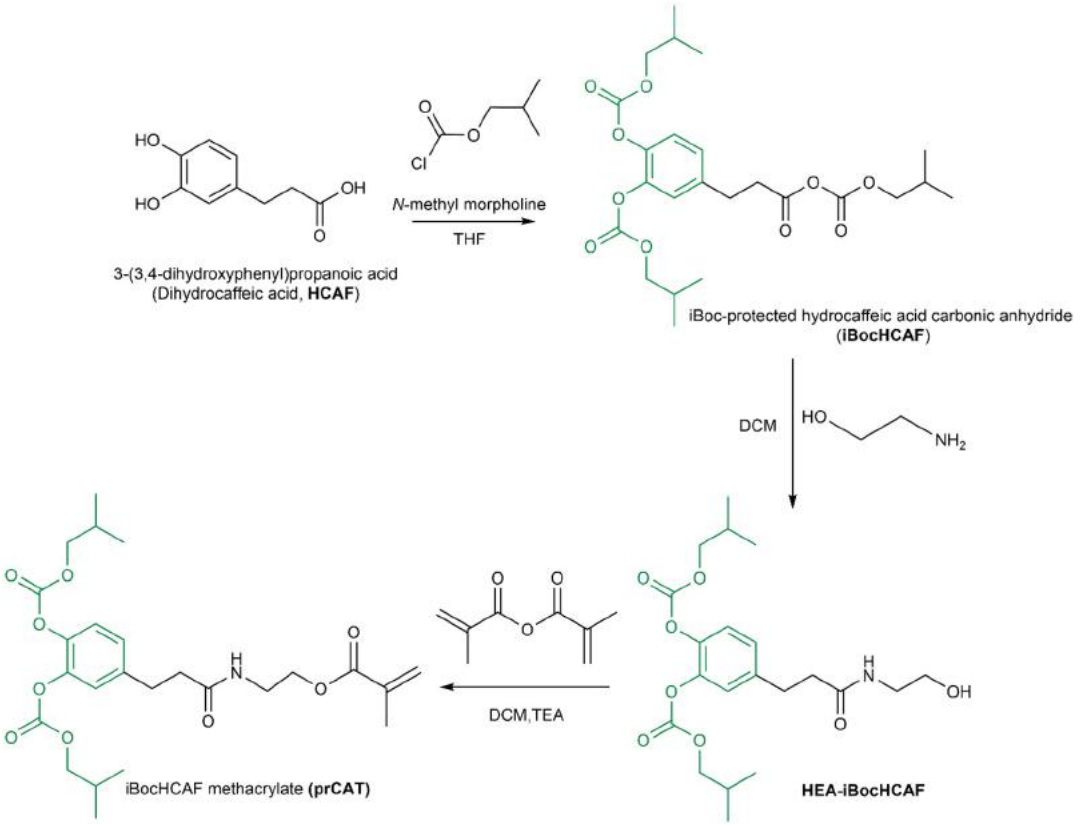

Scheme 1 Schematic representation of the three-step synthesis route of iBocDHCA methacrylate as the protected catechol (prCAT) monomer.

ppm: 167.1 (C), 153.0 (C), 152.9 (C), 149.1 (C), 142.6 (C), 141.3 (C), 138.6 (C), 126.7 (CH), 123.3 (CH), 123.1 (CH), 75.7 (CH_2), 75.3 (CH_2), 75.2 (CH_2), 35.6 (CH_2), 29.7 (CH_2), 27.9 (CH), 27.7 (CH), 18.9 × 2 (CH_3). Refer to Fig. S2† for ^{1}H NMR peak assignments.

2.3.2. Step (2) 4-(3-((2-hydroxyethyl)amino)-3-oxopropyl)-1,2-phenylene diisobutyl bis(carbonate), (iBocDHCA-HEA). To an ice-cooled and stirring solution of iBocDHCA (2.9 g, 6.0 mmol) in DCM (130 mL), was added dropwise, in three portions, ethanolamine (363 μL, 367 mg, 6.0 mmol) under nitrogen. After stirring for 3 h at room temperature, the solvent and excess reagents were removed under vacuum. The resulting crude oil was purified by silica gel flash chromatography with the gradient solvent system, 1 : 1 EtOAc/DCM → 5% methanol (MeOH) in 1 : 1 EtOAc/DCM (v/v) to afford the product 4-(3-((2-hydroxyethyl)amino)-3-oxopropyl)-1,2-phenylene diisobutyl bis(carbonate), iBocDHCA-HEA, as a clear oil (3.1 g, 60% yield). ^{1}H NMR (400 MHz, $CDCl_3$) δ ppm: 7.18–7.10 (3H, m, ArH), 5.90 (1H, br s, –CONH–), 4.02 (4H, d, J = 6.2 Hz, 2 × CH_2, isobutyl), 3.46 (2H, t, J = 6.0 Hz, CH_2), 3.29–3.25 (2H, m, CH_2), 2.98 (2H, t, J = 7.1 Hz, CH_2), 2.47 (2H, t, J = 7.0 Hz, CH_2), 2.09–1.98 (3H, m, CH, isobutyl), 0.98 (12H, dd, J = 6.8 Hz, J = 1.2 Hz, 4 × CH_3, isobutyl). Refer to Fig. S3† for ^{1}H NMR peak assignments.

2.3.3. Step (3) 2-((3-(3,4-bis((isobutoxycarbonyl)oxy)phenyl) propanoyl)oxy)ethyl methacrylate (prCAT monomer). To an ice-cooled solution of 4-(3-((2-hydroxyethyl)amino)-3-oxopropyl)-1,2-phenylene diisobutyl bis(carbonate) (2.0 g, 4.8 mmol) and TEA (1.0 mL, 0.74 g, 7.3 mmol) in dry DCM (120 mL), was added methacrylic anhydride dropwise (0.97 g, 0.94 mL, 6.3 mmol) under nitrogen. The reaction mixture was left stirring under nitrogen overnight at room temperature. The reaction mixture was then diluted with more DCM and washed successively with 0.2 M HCl (2×), water (2×), saturated aqueous sodium bicarbonate (2×), water (2×), and saturated brine (1×). The organic phase was then dried with $MgSO_4$ (anhydrous), and the solvent removed under reduced pressure. The resulting crude oil was purified by silica gel flash chromatography with the gradient solvent system, 1 : 1 EtOAc/DCM → 5% MeOH in 1 : 1 EtOAc/DCM (v/v) affording the product, iBocDHCA methacrylate (prCAT monomer), as a clear, colourless oil (1.9 g, 70%). ^{1}H NMR (400 MHz, $CDCl_3$) δ ppm: 7.18–7.06 (3H, m, ArH), 6.10–6.09 (m, 1H, =CH), 5.90 (1H, br s, –CONH–), 5.59–5.58 (m, 1H, =CH), 4.19 (2H, t, J = 6.0 Hz, CH_2), 4.02 (4H, d, J = 6.2 Hz, 2 × CH_2, isobutyl), 3.53 (2H, dt, J = 10.9, 5.6 Hz, CH_2), 2.46 (2H, t, J = 7.7 Hz, CH_2), 2.09–1.98 (2H, m, CH, isobutyl), 1.96–1.89 (3H, m, –CH_3C=CH_2), 0.98 (12H, dd, J = 6.7, 1.7 Hz, 4 × CH_3, isobutyl).

^{13}C NMR (100 MHz, $CDCl_3$) δ ppm: 171.9 (C), 167.6 (C), 153.1 (C), 153.0 (C), 142.5 (C), 141.0 (C), 140.1 (C), 136.1 (C), 126.8 (CH), 126.2 (CH), 123.1 (C), 123.0 (CH), 75.2 (CH_2), 75.2 (CH_2), 63.6 (CH_2), 39.0 (CH_2), 38.1 (CH_2), 31.0 (CH_2), 27.9 (CH), 27.9 (CH), 18.9 × 2 (CH_3), 18.4 (CH_2). Refer to Fig. S4† for ^{1}H NMR peak assignments.

2.4. Synthesis of the stabilising agents ($P(OEGMA)_x$-*b*-$P(CAT)_y$)

A typical reversible addition–fragmentation chain-transfer (RAFT) polymerisation methodology was employed to synthesise $P(OEGMA)_x$-*b*-$P(CAT)_y$ through the following 4-step procedure (Scheme 2 and Tables S2, S3†):

2.4.1. Step (1) polymerisation of $P(OEGMA)_{25}$ and $P(OEGMA)_{55}$. Briefly, appropriate amounts of $OEGMA_{500}$, CPBD RAFT agent, and AIBN initiator were dissolved in toluene to yield homogenous mixtures with the stoichiometries of $[CPBDT]_0 : [OEGMA]_0 : [AIBN]_0 = 1 : 50 : 0.15$ (for $P(OEGMA)_{25}$) and $[CPBDT]_0 : [OEGMA]_0 : [AIBN]_0 = 1 : 100 : 0.15$ (for $P(OEGMA)_{55}$). The obtained mixtures were then deoxygenated for 25 min *via* sparging with N_2 and placed in a pre-heated oil bath at 70 °C while stirring. The polymerisation reactions were performed for 6 and 10 h for $P(OEGMA)_{25}$ (**1a**) and $P(OEGMA)_{55}$ (**1b**), respectively. Afterwards, each polymerisation was stopped by cooling down the reaction mixture and

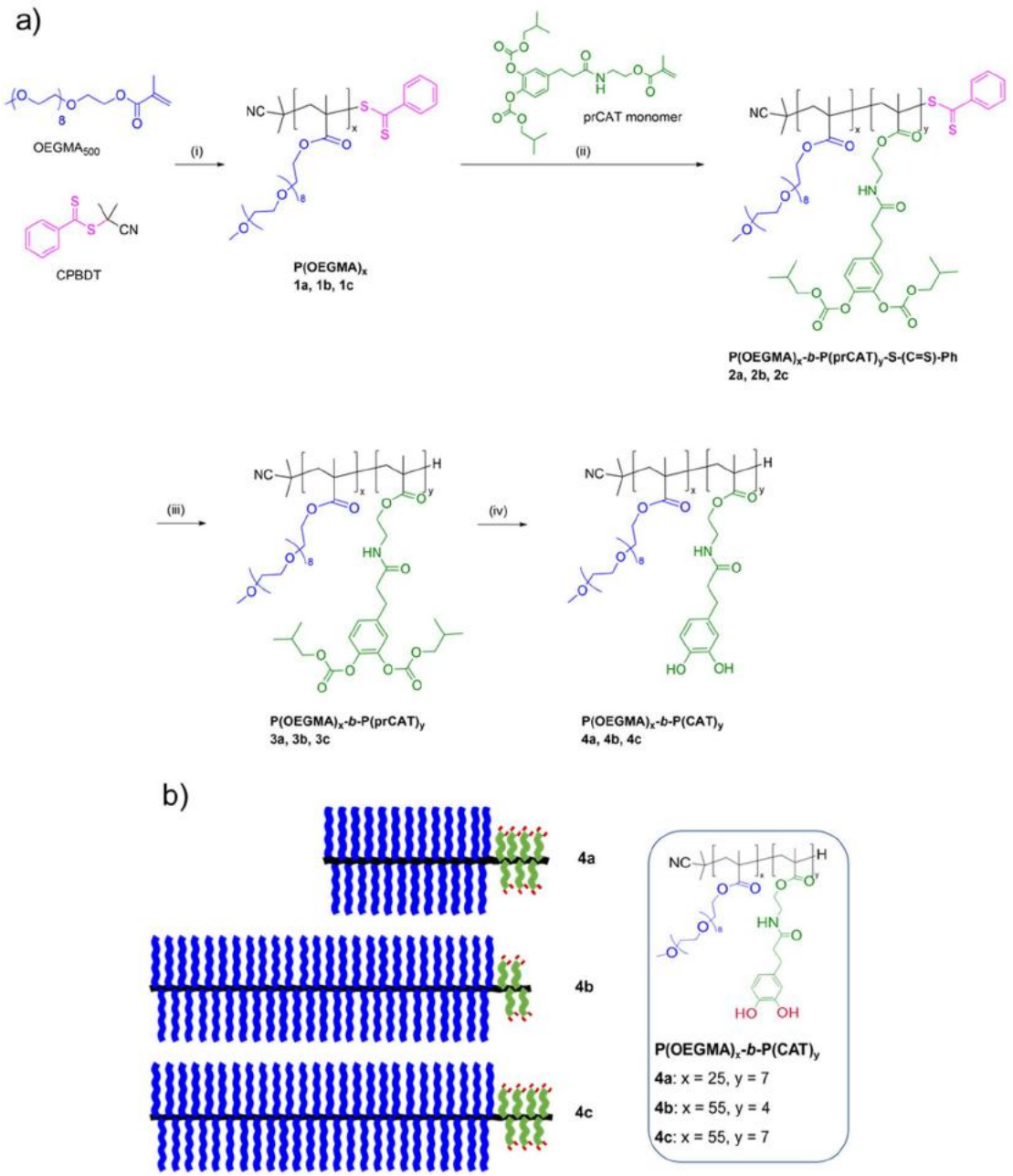

Scheme 2 a) Synthesis route for the stabilising agents ($P(OEGMA)_x$-*b*-$P(CAT)_y$): (i) AIBN, toluene, 70 °C (**1a**: t = 6 h, x = 25 and **1b**: t = 10 h, x = 55); (ii) AIBN, acetonitrile, 70 °C (**2a**: t = 4 h, x = 25; **2b**: t = 3.4 h, x = 55; **2c**: t = 5 h, x = 55); (iii) ACHN, EPHP, dioxane, 100 °C (**3a**: t = 2 × 2 h, x = 25; **3b**: t = 2 h, x = 55; **3c**: t = 3 × 2 h); (iv) IPAM, TEA, DCM, room temperature, 16 h. (b) Graphical representation of the synthesised stabilising agents with various hydrophilic block (*i.e.*, P(OEGMA)) and anchoring block (*i.e.*, (CAT)) chain lengths.

subsequently exposing to air. The overall monomer conversion was determined by ^{1}H NMR ($CDCl_3$) to be ~50% and ~55% for $P(OEGMA)_{25}$ and $P(OEGMA)_{55}$, respectively. The resonances integrated to obtain conversions for OEGMA were the vinyl peaks at 5.4 and 5.9 ppm (monomer only) and the OCH_2-peaks at 3.8–4.1 ppm (monomer and polymer). The obtained products were purified *via* precipitation (6 times) in petroleum benzine/diethyl ether mixture (4 : 1, v/v) to remove all traces of unreacted monomer, and the residual solvent was then removed under airflow overnight. The final products of $P(OEGMA)_{25}$ (1 g = 50% yield) and $P(OEGMA)_{55}$ (1 g = 50% yield) were analysed *via* ^{1}H NMR ($CDCl_3$) and SEC (DMAc) (Fig. S5–6, S16–17 and Table S3†).

2.4.2. Step (2) block extension procedure using prCAT monomer. Briefly, $P(OEGMA)_{25}$ or $P(OEGMA)_{55}$ macro RAFT agent, prCAT monomer, and AIBN initiator were dissolved in acetonitrile (ACN) to yield homogenous mixtures with the stoichiometries of $[P(OEGMA)_{25}]_0 : [prCAT]_0 : [AIBN]_0 = 1 : 15 : 0.15$, $[P(OEGMA)_{55}]_0 : [prCAT]_0 : [AIBN]_0 = 1 : 15 : 0.20$, and $[P(OEGMA)_{55}]_0 : [prCAT]_0 : [AIBN]_0 = 1 : 15 : 0.20$ to provide $P(OEGMA)_{25}$-*b*-P(prCAT)$_7$-S-(C═S)-Ph (**2a**), $P(OEGMA)_{55}$-*b*-P(prCAT)$_4$-S-(C═S)-Ph (**2b**), and $P(OEGMA)_{55}$-*b*-P(prCAT)$_7$-S-(C═S)-Ph (**2c**), respectively. Next, the reaction mixtures were deoxygenated for 15 min *via* sparging with N_2, placed in a preheated oil bath at 70 °C, and stirred for 4 h, 3.4 h, and 5 h for **2a**, **2b**, and **2c**, respectively. Thereafter, each reaction mixture was allowed to cool down and then exposed to ambient air in order to halt the polymerisation. The monomer conversion was determined by ^{1}H NMR ($CDCl_3$) to be ~50%, ~30%, and ~50% for **2a**, **2b**, and **2c**, respectively. The conversions were determined by integrating the resonances of the vinyl peaks at 5.4 and 5.9 ppm (monomer only) and the CH_2-peaks at 2.46 ppm (monomer and polymer). The resulting products were then purified *via* 3 cycles of precipitation in petroleum benzine/diethyl ether mixture (4 : 1, v/v) to remove all traces of unreacted reagents, and the residual solvents were removed under vacuum. The final products of step 2 were analysed using ^{1}H NMR ($CDCl_3$) and SEC (DMAc) (Fig. S7–9, S16–18 and Table S3†).

2.4.3. Step (3) RAFT end group removal. In brief, $P(OEGMA)_{25}$-*b*-P(prCAT)$_7$-S-(C═S)-Ph, $P(OEGMA)_{55}$-*b*-P(prCAT)$_4$-S-(C═S)-Ph, or $P(OEGMA)_{55}$-*b*-P(prCAT)$_7$-S-(C═S)-Ph, 1-ethylpiperidine hypophosphite (EPHP) H-donor, and ACHN radical initiator were dissolved in dioxane to yield homogenous mixtures with the stoichiometries of $[P(OEGMA)_{25}$-*b*-P(prCAT)$_7$-S-(C═S)-Ph$]_0 : [EPHP]_0 : [ACHN]_0 = 1 : 10 : 0.4$, $[P(OEGMA)_{55}$-*b*-P(prCAT)$_4$-S-(C═S)-Ph$]_0 : [EPHP]_0 : [ACHN]_0 = 1 : 10 : 0.45$, and $[P(OEGMA)_{55}$-*b*-P(prCAT)$_7$-S-(C═S)-Ph$]_0 : [EPHP]_0 : [ACHN]_0 = 1 : 10 : 0.45$ to yield $P(OEGMA)_{25}$-*b*-P(prCAT)$_7$ (**3a**), $P(OEGMA)_{55}$-*b*-P(prCAT)$_4$ (**3b**), and $P(OEGMA)_{55}$-*b*-P(prCAT)$_7$ (**3c**), respectively. Next, the prepared mixtures were deoxygenated for 5 min with N_2 sparging, placed in a preheated oil bath at 100 °C and stirred for 2 × 2 h, 2 h, and 3 × 2 h for **3a**, **3b**, and **3c**, respectively. The radical-induced reduction process[19] was ceased by cooling down each reaction mixture to room temperature. The reaction progress was monitored by SEC by comparing the detected maximum intensities measured by refractive index (RI) and UV (at wavelength of 310 nm) before and after the end-group removal procedure (Table S2†), and using the post-cleavage to pre-cleavage ratio to indicate the percentage conversion.[19] Upon progress of each reaction to around 90% conversion, the obtained product was purified *via* dialysis (molecular weight cut off (MWCO) of 3500 g mol^{-1}) against acetone (24 h), acetone/Milli-Q water (50 : 50, 24 h), and Milli-Q water (24 h) to remove the products of end-group removal and the hypophosphite salt. The final decolourised products were then freeze dried from water and analysed by ^{1}H NMR ($CDCl_3$) and SEC (DMAc) (Fig. S10–12, S16–18 and Table S3†).

2.4.4. Step (4) isobutyl carbonate deprotection. $P(OEGMA)_{25}$-*b*-P(prCAT)$_7$, $P(OEGMA)_{55}$-*b*-P(prCAT)$_4$, or $P(OEGMA)_{55}$-*b*-P(prCAT)$_7$ and dry TEA (2 equivalents per carbonate group of the prCAT block as a sacrificial counter-base for the catechol units) were first dissolved in dry DCM. The resulting mixture of each copolymer was deoxygenated with N_2 sparging for 3 min and kept under N_2. Dry DCM (2.7 mL) and IPAM (1.3 mL) were then mixed to produce a 33% v/v solution that was deoxygenated with N_2 for 5 min. Thereafter, an aliquot of the IPAM in DCM solution was transferred dropwise into the polymer solution, so that the final concentration of IPAM in DCM was ~12% v/v (~1.5 M) (*i.e.*, approximately 20 equivalents of IPAM per isobutyl carbonate-protected catechol). The stoichiometry of each reaction mixture was $[P(OEGMA)_{25}$-*b*-P(prCAT)$_7]_0 : [TEA]_0 : [IPAM]_0 = 1 : 28 : 140$, $[P(OEGMA)_{55}$-*b*-P(prCAT)$_4]_0 : [TEA]_0 : [IPAM]_0 = 1 : 16 : 80$, and $[P(OEGMA)_{55}$-*b*-P(prCAT)$_7]_0 : [TEA]_0 : [IPAM]_0 = 1 : 28 : 140$, yielding $P(OEGMA)_{25}$-*b*-P(CAT)$_7$ (**4a**), $P(OEGMA)_{55}$-*b*-P(CAT)$_4$ (**4b**), and $P(OEGMA)_{55}$-*b*-P(CAT)$_7$ (**4c**), respectively. The deprotection reaction was performed under N_2 overnight at room temperature. Each polymer was then precipitated in a mixture of petroleum benzine and diethyl ether (4 : 1, v/v) three times, dissolved in 0.1 M HCl, dialysed for 48 h against 0.1 M HCl (MWCO of 3500 g mol^{-1}), and freeze dried. The final products were analysed by ^{1}H NMR ($CDCl_3$ for **4a**, DMSO-d_6 for **4b** and **4c**) and SEC (DMAc) (Fig. S13–15, S16–18 and Table S3†). As indicated, two characteristic peaks corresponding to the isobutyl carbonate groups in the ^{1}H NMR spectrum (*i.e.*, δ 0.96 and 3.99 ppm) were absent following deprotection.

2.5. Fabrication of $P(OEGMA)_x$-*b*-$P(CAT)_y$ coated NC ($P(OEGMA)_x$-*b*-$P(CAT)_y$-NC)

Bare NC were coated by $P(OEGMA)_x$-*b*-$P(CAT)_y$ by the following method. Firstly, to a dispersion of bare NC in Milli-Q water (0.5 mg mL^{-1}) (prepared *via* high-speed vortex), was dropwise added a solution of $P(OEGMA)_x$-*b*-$P(CAT)_y$ in MeOH (15 mg mL^{-1}) while stirring at 1000 rpm. The pale yellow colour of the bare NC dispersion instantly changed to pale violet upon addition of polymer solution, and the reaction was then left to stir overnight at room temperature. Next, the polymer-coated NPs were isolated *via* centrifugation at 6000 rpm for 5 min and washed with MeOH, followed by centrifugation at 3000 rpm for 5 min to remove any traces of unattached copolymer. The

washing procedure was repeated a further two times with MeOH and once more with Milli-Q water. The obtained particles were readily redispersed in Milli-Q water and freeze dried to yield the final product of P(OEGMA)$_{25}$-*b*-P(CAT)$_7$-NC, P(OEGMA)$_{55}$-*b*-P(CAT)$_4$-NC, or P(OEGMA)$_{55}$-*b*-P(CAT)$_7$-NC (yield ~70%) as a pale violet powder. The above procedure is illustrated in Fig. S19.† Grafting densities were then calculated based on TGA results using the following formula:[20,21]

$$\text{Grafting density} = \frac{S_{spe}}{M_{gr} \times N_A} \times \frac{W_{tot} - W_{ref}}{100 - (W_{tot} - W_{ref})} \quad (1)$$

where S_{spe} is the specific surface (nm^2 g^{-1}) of the NC, M_{gr} is the molar mass of the grafted copolymer, N_A is Avogadro's constant, W_{tot} is the weight loss of the grafted copolymer, and W_{ref} the weight loss of the reference sample (*i.e.*, NC).

Also, to approximate the difference in brush height for each P(OEGMA)$_x$-*b*-P(CAT)$_y$-NC sample, the following correlation was derived, assuming (i) a linear polymer structure, (ii) a spherical grafting surface, (iii) good solvent medium, and (iv) large curvature:[22]

$$H \sim \left(\frac{3}{5} N^3 R^2 \sigma\right)^{\frac{1}{5}} \quad (2)$$

where H is the brush height, N is the molecular weight of the grafted copolymer, R is the radius of the grafting surface, and σ is the grafting density.

2.6. Colloidal stability analysis for bare and P(OEGMA)$_x$-*b*-P(CAT)$_y$-NC samples

The colloidal stability of bare and P(OEGMA)$_x$-*b*-P(CAT)$_y$-NC samples was investigated based on a previous study as follows.[23] Firstly, a dispersion of each sample at a NC concentration of 100 μg mL^{-1} (calculated for P(OEGMA)$_x$-*b*-P(CAT)$_y$-NC samples based on TGA results) was prepared in PBS (1×, pH 7.4) *via* high-speed vortex, and the UV-Vis absorbance of Ce^{4+} was measured at λ_{max} values in the ranges of 316–300 nm (for bare NC), 300–293 nm (for P(OEGMA)$_{25}$-*b*-P(CAT)$_7$-NC), 302–299 nm (for P(OEGMA)$_{55}$-*b*-P(CAT)$_4$-NC), and 302–298 nm (for P(OEGMA)$_{55}$-*b*-P(CAT)$_7$-NC)[24] at time intervals of 1 h, 2 h, 4 h, 6 h, 24 h, and 48 h at room temperature without disturbing the dispersion inside the cuvette. Of note, λ_{max} changed at each time interval due to occurrence of a blue-shift.

Colloidal stability for bare NC and P(OEGMA)$_{55}$-*b*-P(CAT)$_4$-NC was also examined in PBS (10×, pH 7.4) medium at time intervals of 2 min, 4 min, 6 min, 8 min, and 10 min using the same protocol, with the UV-Vis absorbance of Ce^{4+} measured at λ_{max} of 340 nm (for bare NC) or 323 nm (for P(OEGMA)$_{55}$-*b*-P(CAT)$_4$-NC).

2.7. Antioxidant activity analysis

2.7.1. CAT-like activity. CAT-like activity was assessed using a previously reported fluorescent spectroscopy method.[25] Bare and P(OEGMA)$_x$-*b*-P(CAT)$_y$-NC samples (at a NC concentration of 100 μg mL^{-1}) were mixed with H_2O_2 (400 mM) in PBS (1×, pH 7.4) *via* high-speed vortex and incubated at room temperature for 6 h. Positive and negative controls were prepared in the absence of NC-based nanoparticles and H_2O_2, respectively. Over the incubation time, H_2O_2 decomposes to OH$^\bullet$ radicals, unless eliminated by the potential CAT-like activity of bare and P(OEGMA)$_x$-*b*-P(CAT)$_y$-NC samples. Next, 1.5 mM of TA in dimethylformamide (DMF) was added to each mixture followed by vigorous mixing. TA reacts with OH$^\bullet$ radicals to yield a fluorescent 2-hydroxyterephthalic acid product. CAT-like activity was then determined based on the fluorescent intensity of 2-hydroxyterephthalic acid (excited at 320 nm) for each sample relative to that of the positive control.

2.7.2. SOD-like activity. SOD-like activity was analysed *via* fluorescence spectroscopy using a HE probe as previously described by Liu *et al.*[26] Briefly, 1.2 mM of X and 0.2 U mL^{-1} of XO, along with bare and P(OEGMA)$_x$-*b*-P(CAT)$_y$-NC samples (at NC concentration of 100 μg mL^{-1}), were thoroughly mixed in PBS (10×, pH 7.4) and incubated at 37 °C for 10 min. Positive and negative controls were prepared in the absence of NC-based nanoparticles and XO, respectively. During incubation, reaction of X and XO generates $O_2^{\bullet-}$ radicals which would be quenched by the potential SOD-like activity of bare and P(OEGMA)$_x$-*b*-P(CAT)$_y$-NC samples. Afterwards, 100 μg mL^{-1} of HE in dry dimethyl sulfoxide (DMSO) was added to each mixture and incubated for another 10 min. Residual $O_2^{\bullet-}$ radicals oxidise HE to its fluorescent form, enabling measurement of SOD-like activity by comparing the fluorescent intensity of oxidised HE (excited at 470 nm) for each sample relative to that of positive control.

2.8. Cell culture

Normal human embryonic kidney (HEK293) cells, procured from the American Type Culture Collection (ATCC), were grown in high glucose DMEM media supplemented with 10% (v/v) FBS and incubated under a humidified atmosphere containing 5% CO_2 at 37 °C. Cells were passaged (up to a passage number of 30) once 70–80% confluency was achieved applying trypsin EDTA. For the cytotoxicity assay, cells were seeded at a density of 30 000 cells per well using 96-well plates.

2.9. Cytotoxicity assay

Cytotoxicity of bare and P(OEGMA)$_x$-*b*-P(CAT)$_y$-NC samples against HEK293 cells was studied by an Alamar Blue assay. Briefly, the cells were first incubated for 24 h on a 96-well plate, and then treated with each sample pre-dispersed in media at a NC concentration of 100 μg mL^{-1}. After 24 h of treatment, media containing the NC-based nanoparticles was replaced by 100 μL of the Alamar Blue solution in media (1 : 10 (v/v)). After 2.5 h, the fluorescence intensity of each well was measured using a CLARIOstar microplate reader (BMG LABTECH) at excitation and emission wavelengths of 530 and 590 nm, respectively. To ensure reproducibility of the results, three independent experiments each comprising three technical replicates were performed, and the cell viability (%) was determined as a ratio of the fluorescence intensity of treated cells to that of non-treated cells (negative control, −Ctrl). Also,

10% (v/v) ethanol 80% was used as the positive control (+Ctrl) with <10% viability.

3. Results and discussion

3.1. Design and synthesis of the block copolymer stabilising agent

In order to colloidally stabilise metal oxide nanoparticles in biological media, a suitable stabilising agent should include an anchoring block, to provide a stable connection to the nanoparticle surface, and a hydrophilic block, to prevent/mitigate aggregate formation. A variety of anchoring functionalities have previously been proposed to bond with the surface of NC, *e.g.*, phosphonic acid,[16] acrylic acid,[27] ethoxy silane,[28] and amine.[29] Herein, catechol functionality was employed, as these structures exhibit a strong affinity to metal oxide nanoparticles *via* three major types of bidentate bonding mechanism, *i.e.*, bidentate chelating bonding, bidentate bridging bonding (inner sphere), and bidentate bridging bonding (outer sphere).[30] Additionally, poly(oligo(ethylene glycol) methyl ether methacrylate) (P(OEGMA)) was chosen as the hydrophilic block to improve the colloidal stability of NC, primarily through a steric repulsion mechanism. P(OEGMA) is a non-linear analogue of polyethylene glycol (PEG), and P(OEGMA)-based homo- and copolymers have been extensively studied for biomedical applications due to their appealing properties, *e.g.*, excellent structural versatility and stability, low-fouling/stealth properties, and biocompatibility.[31,32] In this study, a novel catecholate monomer, *i.e.*, iBoc-protected dihydrocaffeate methacrylate (protected catechol; prCAT), was synthesised through a three-step reaction (Scheme 1), and a block section comprised of this monomer was added to a RAFT-synthesised P(OEGMA) *via* chain extension (Scheme 2). Deprotection of iBoc groups using amine then yielded a block of catechol units, P(CAT). This approach afforded control over the number of catechol units and thus enabled evaluation of the effect of increasing the number of catechol units on copolymer binding to the surface of NC. Also, to further understand the effect of block copolymer composition on colloidal stability and antioxidant properties of NC, the (CAT) : (OEGMA) ratio was varied.

3.1.1. Synthesis of the protected catechol (prCAT) monomer. Protection strategies for the catechols were implemented both to minimise side reactions during synthesis of the monomer, and to avoid potential impacts on the polymerisation by catechols. To provide the catechol-functional monomer, the mixed carbonic anhydride of dihydrocaffeic acid, iBocDHCA, was first formed by reacting dihydrocaffeic acid (DHCA) with isobutyl chloroformate (Scheme 1, step 1). In this structure, both hydroxyls of the catechol moiety were acyl-protected (as isobutyl carbonate groups), while the carboxylic acid was activated as a carbonic anhydride. Subsequent reaction with ethanolamine yielded 4-(3-((2-hydroxyethyl)amino)-3-oxopropyl)-1,2-phenylene diisobutyl bis(carbonate), HEA-iBocDHCA, *via* the selective reaction of the amine with the activated carbonic anhydride (Scheme 1, step 2). Methacrylation of the hydroxyl group gave iBocDHCA methacrylate, the protected catechol (prCAT) monomer (Scheme 1, step 3). This monomer differs from the one previously reported by us in that it contains an ester bond in between the protected catechol and the methacrylate groups.[33] The synthesized iBocDHCA, iBocDHCA-HEA, and iBocDHCA methacrylate were characterized by NMR spectroscopy (Fig. S2–S4†).

3.1.2. Synthesis of block copolymer stabilizing agents P(OEGMA)$_x$-*b*-P(CAT)$_y$. As depicted in Scheme 2, the first step in synthesizing the library of block copolymer stabilizing agents (P(OEGMA)$_x$-*b*-P(CAT)$_y$) was to polymerize OEGMA$_{500}$ *via* RAFT to obtain hydrophilic blocks of P(OEGMA)$_{25}$ (**1a**) and P(OEGMA)$_{55}$ (**1b**) (Fig. 1). Obtaining two hydrophilic blocks of disparate chain length enabled subsequent investigation of the effect of chain length on colloidal stability. Next, P(OEGMA)$_{25}$ was chain extended with a block of 7 prCAT units (**2a**), while P(OEGMA)$_{55}$ was chain extended with a block of 4 prCAT units (**2b**) and a block of 7 prCAT units, respectively (**2c**). This led to a small library of copolymers with differing number of anchoring units, as verified by ^{1}H NMR and SEC analyses (Fig. S7–S9 and S16–S18†). To avoid complications during the deprotection step arising from aminolysis of the thiocarbonylthio groups, the benzodithioate RAFT end-group was removed through a radical-induced reduction reaction using EPHP and ACHN,[19] which was monitored by SEC with UV detection as well as ^{1}H NMR spectroscopy (Table S2; Fig. S10–12†), yielding P(OEGMA)$_x$-*b*-P(prCAT)$_y$, **3a**, **3b**, and **3c**. Deprotection of the prCAT units was then performed using a small molecule amine (isopropyl amine, IPAM) under deoxygenated and dry conditions to minimise oxidation of catechol units. The deprotection yielded a small molecule carbamate (Scheme S1†) that was removed *via* precipitation of the polymer into a mixture of diethyl ether and petroleum benzine. Following deprotection and precipitation of the polymers, they were then dissolved in 0.1 M HCl to protonate the catecholate groups and minimise oxidation, and dialysed under mildly acidic aqueous conditions to further remove

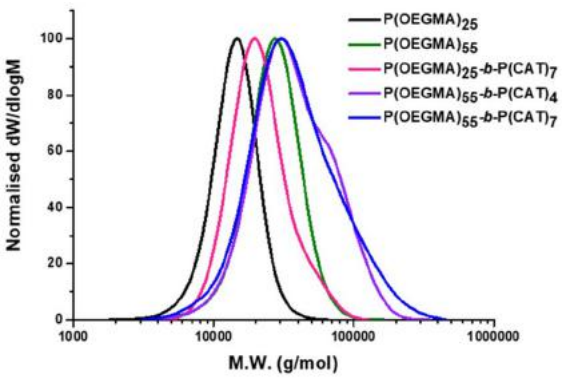

Fig. 1 SEC (DMAc) molecular weight distribution graphs of the starting hydrophilic blocks (*i.e.*, P(OEGMA)$_{25}$ (**1a**) and P(OEGMA)$_{55}$ (**1b**)) as well as the synthesised stabilising agents including P(OEGMA)$_{25}$-*b*-P(CAT)$_7$ (**4a**), P(OEGMA)$_{55}$-*b*-P(CAT)$_4$ (**4b**), and P(OEGMA)$_{55}$-*b*-P(CAT)$_7$ (**4c**).

impurities (such as salts and carbamate).[19] The obtained final products of P(OEGMA)$_{25}$-*b*-P(CAT)$_7$ (**4a**), P(OEGMA)$_{55}$-*b*-P(CAT)$_4$ (**4b**), and P(OEGMA)$_{55}$-*b*-P(CAT)$_7$ (**4c**) were characterized by SEC (Fig. 1) and ^{1}H NMR analyses (Fig. S13–S15†). As summarised in Table S3,† the SEC dispersity indexes of the synthesised block copolymers were 1.26, 1.49, and 1.68 for **4a**, **4b**, and **4c**, respectively. Peak broadening of the SEC traces was observed across the series which manifested after the deprotection step. This could be due to the interaction of the catechol hydroxyl groups with the SEC column during analysis and/or oxidative coupling of catechol units, which could result in the appearance of high molecular weight shoulders in the SEC traces and thus lead to an increase in dispersity. Notably, the broadening was more significant for **4b** and **4c** which contained a longer P(OEGMA) block (55 units), rather than correlating with the number of catechol units. Despite the tailing and broadening, the solubility of the copolymers was not affected, and there was no significant change in colour to yellow-brown which would indicate significant oxidative coupling and crosslinking.[34]

3.2. Fabrication of P(OEGMA)$_x$-*b*-P(CAT)$_y$ coated NC (P(OEGMA)$_x$-*b*-P(CAT)$_y$-NC)

NC were coated with P(OEGMA)$_x$-*b*-P(CAT)$_y$ *via* a grafting-to technique which allowed direct comparison between bare and copolymer coated NC. Specifically, by using this approach neither the physicochemical properties of the core NC could affect the properties of the produced stabilising agent (as might occur in the case of a grafting-from technique), nor could the polymerisation conditions impact the structural properties of the core NC (which could be the case if a grafting-from technique was applied).[35] Indeed, by applying the grafting-to technique, we were able to produce the copolymers independent of the core NC, thereby ameliorating any potential impact of the NC on the characteristics of the final P(OEGMA)$_x$-*b*-P(CAT)$_y$ copolymers. Commercially-sourced NC was employed to keep the core nanoparticle properties constant across all investigations. After polymerisation, deprotection of prCAT repeating units yielded active catechol units that bind to the surface of NC *via* bidentate bonding mechanisms.[30] Of note, Mitchell *et al.* have shown in detail that only the Ce^{4+} ions at the edges of the NC crystal facets are involved in the mentioned bidentate bonding interactions.[36]

3.2.1. Characterisation of bare and P(OEGMA)$_x$-*b*-P(CAT)$_y$-NC. DLS analysis was employed to probe the impact of copolymer coating on the hydrodynamic size (by number) and size distribution of P(OEGMA)$_x$-*b*-P(CAT)$_y$-NC samples dispersed in Milli-Q water. As depicted in Fig. 2a, the mean diameters (derived from Number PSD curves) and polydispersity indices (PdI) were respectively measured to be 141 nm (PdI 0.33), 128 nm (PdI 0.42), 79 nm (PdI 0.39), and 173 nm (PdI 0.57) for bare NC, P(OEGMA)$_{25}$-*b*-P(CAT)$_7$-NC, P(OEGMA)$_{55}$-*b*-P(CAT)$_4$-NC, and P(OEGMA)$_{55}$-*b*-P(CAT)$_7$-NC. Further, TEM analysis was performed to measure the size of the samples in the dry state, with mean diameters determined to be 15 nm, 17 nm, 19 nm, and 20 nm for bare NC, P(OEGMA)$_{25}$-*b*-P(CAT)$_7$-NC, P(OEGMA)$_{55}$-*b*-P(CAT)$_4$-NC, and P(OEGMA)$_{55}$-*b*-P(CAT)$_7$-NC, respectively (Fig. 2b and S20†). Also, the TEM images for bare NC exhibited an irregularity in shape that was also observed for the P(OEGMA)$_x$-*b*-P(CAT)$_y$-NC samples (Fig. S20†).

A significant difference between the mean diameters measured by DLS and TEM analyses was observed, potentially arising from hydration of the nanoparticles during DLS analysis,[37] or resulting from possible dynamic aggregations/agglomerations in water over the course of DLS measurement.[38] Further, of the DLS results, only P(OEGMA)$_{55}$-*b*-P(CAT)$_4$-NC showed a significant decrease in size as compared to bare NC, which may result from the improved dispersal of nanoparticles upon stabilisation by P(OEGMA)$_{55}$-*b*-P(CAT)$_4$. In contrast, both P(OEGMA)$_{25}$-*b*-P(CAT)$_7$-NC and P(OEGMA)$_{55}$-*b*-P(CAT)$_7$-NC exhibited an increase in hydrodynamic size that could stem from ~2-fold more anchoring units and thus the possibility of interaction of catechol groups with more than one NC occurring simultaneously, leading to aggregation. Further, P(OEGMA)$_{55}$-*b*-P(CAT)$_4$-NC showed the smallest increase in PdI that could indicate a more even distribution of coating for P(OEGMA)$_{55}$-*b*-P(CAT)$_4$ compared to P(OEGMA)$_{25}$-*b*-P(CAT)$_7$ and P(OEGMA)$_{55}$-*b*-P(CAT)$_7$. On the other hand, the TEM results did not indicate an increase in size to suggest that the addition of P(OEGMA)$_x$-*b*-P(CAT)$_y$ coating to NC led to aggregation. Since the boundary between adjacent nanoparticles was still observable in TEM images it could instead suggest that it was agglomeration of P(OEGMA)$_x$-*b*-P(CAT)$_y$-NC, which could have taken place during sample preparation.[39] Further, particularly in the cases of P(OEGMA)$_{25}$-*b*-P(CAT)$_7$ and P(OEGMA)$_{55}$-*b*-P(CAT)$_7$, the dense, hydrated layers of P(OEGMA) might overlap upon drying the samples prior to TEM analysis, emphasising the irregularities observed for the core NC (Fig. S20a†). Of note, ImageJ (1.54f) software was employed to clarify the boundaries of the nanoparticles, although it must be recognised that the final results remain approximate and may be influenced by drying effects. Overall, P(OEGMA)$_x$-*b*-P(CAT)$_y$-NC samples maintained the nanostructure of bare NC, which could potentially benefit their antioxidant activity by maintaining ample surface area for reaction.

Analysis of the zeta potential was carried out to understand whether coating NC with P(OEGMA)$_x$-*b*-P(CAT)$_y$ gave rise to any change in surface charge. As seen in Fig. 2c, zeta potential of bare NC was measured around −32 mV, likely due to the negatively charged hydroxyl groups covering the surface of bare NC in Milli-Q water medium.[27] Significant attenuation of zeta potential for P(OEGMA)$_x$-*b*-P(CAT)$_y$-NC samples relative to bare NC is indicative of interactions with the NC surface. Indeed, the P(OEGMA) block is electrically neutral and thus could shield the surface charge of NC, while the bidentate bonding of catechol units with the surface Ce^{4+} ions could replace the –OH bonding. The residual negative surface charge measured for P(OEGMA)$_x$-*b*-P(CAT)$_y$-NC potentially arises from partial surface coating and/or the hydroxyl functionalities of unattached/free catechol units. Accordingly, P(OEGMA)$_{55}$-*b*-P(CAT)$_4$-NC showed the least negative zeta potential (−3.7 mV)

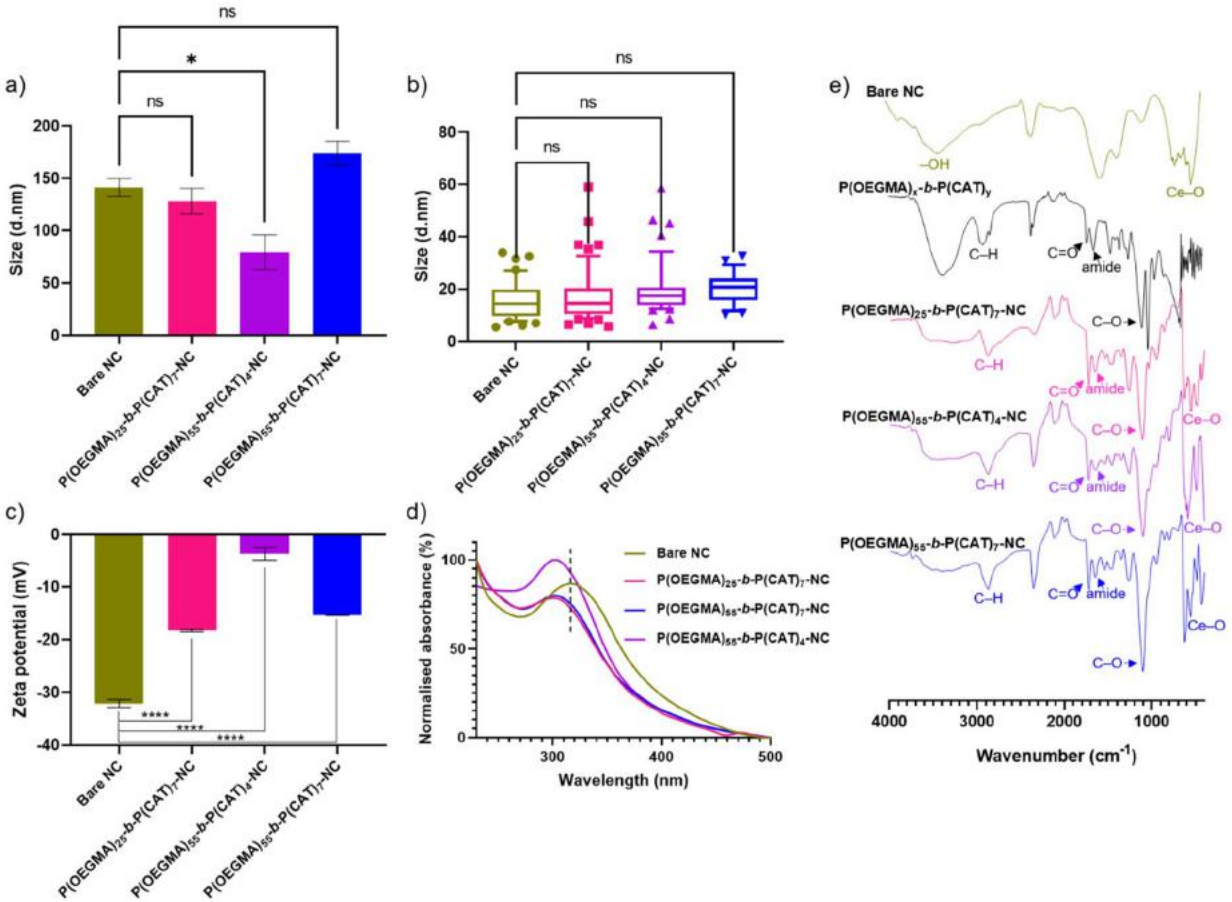

Fig. 2 Structural characterisation of the P(OEGMA)$_x$-*b*-P(CAT)$_y$-NC samples: (a) hydrodynamic size by number determined *via* DLS analysis. (b) Particle size determined through TEM imaging (box plot 10–90 percentile). (c) Surface charge determined by zeta potential analysis. (d) UV-Vis absorbance (normalised by the highest absorbance) illustrating a blue-shift upon addition of the polymer layer to bare NC. (e) ATR-FTIR spectra. The DLS and zeta potential results are reported as mean ± SEM values (n = 3). Statistical significance was calculated *via* ordinary one-way ANOVA with Dunnett's multiple comparisons *post hoc* test (GraphPad Prism 9.0.1) with a 95% confidence interval. ns: not significant, * $P \leq 0.05$, **** $P \leq 0.0001$.

compared to P(OEGMA)$_{25}$-*b*-P(CAT)$_7$-NC (−18.3 mV) and P(OEGMA)$_{55}$-*b*-P(CAT)$_7$-NC (−15.4 mV).

NC structures are reported to show a characteristic UV-Vis absorbance peak with a λ_{max} of around 300–320 nm due to the charge transfer between O 2p and Ce^{4+} 4f bands.[40] Hence, UV-Vis spectrophotometry was used to study whether coating NC with P(OEGMA)$_x$-*b*-P(CAT)$_y$ leads to any optical shift. As shown in Fig. 2d, the observed λ_{max} for bare NC was at around 316 nm, whilst there was a blue-shift of about 14 nm for the P(OEGMA)$_x$-*b*-P(CAT)$_y$-NC. The observed blue-shift potentially results from reduction of Ce^{4+} to Ce^{3+} by the catechol units: a change in valence state of Ce from tetravalent to trivalent increases the charge transfer gap between O 2p and Ce 4f bands and thus leads to a blue-shift.[24] Moreover, the apparent colour change from pale yellow (for bare NC dispersion) to pale violet (for P(OEGMA)$_x$-*b*-P(CAT)$_y$-NC dispersions) (Fig. S19†) is consistent with this blue-shift, as colloidal solutions of Ce_2O_3 have been reported to be pale violet in colour.[40] In addition, Yang *et al.* demonstrated that coating NC with poly(tannic acid) gave rise to an increased concentration of Ce^{3+} due to the reducing activity of tannic acid that has abundant pyrogallol/catechol functional groups.[38]

In order to further validate the coating of the NC surface with P(OEGMA)$_x$-*b*-P(CAT)$_y$, ATR-FTIR analysis was conducted for the freeze-dried samples. As illustrated in Fig. 2e, the spectrum of bare NC showed the characteristic peak attributed to Ce–O stretching at around 506 cm^{-1}, along with the broad peak at around 3400 cm^{-1} related to the stretching of –OH groups on the surface of bare NC.[41] The spectrum of P(OEGMA)$_x$-*b*-P(CAT)$_y$ showed at least four characteristic peaks at around 1090 cm^{-1}, 1640 cm^{-1}, 1720 cm^{-1}, and 2910 cm^{-1} which can be associated with C–O, amide, ester, and C–H bonds respectively in the structure of the synthesised copolymers. Accordingly, the spectra of P(OEGMA)$_{25}$-*b*-P(CAT)$_7$-NC, P(OEGMA)$_{55}$-*b*-P(CAT)$_4$-NC, and P(OEGMA)$_{55}$-*b*-P(CAT)$_7$-NC exhibited the characteristic peaks of bare NC along with those of the P(OEGMA)$_x$-*b*-P(CAT)$_y$, confirming successful coating of NC with the copolymers. Also, it is noteworthy that the spectrum of P(OEGMA)$_x$-*b*-P(CAT)$_y$ showed a strong peak at around 1024 cm^{-1} which could be attributed to C–O stretching of its

alkyl aryl ether (catechol) functionalities, and that this signal was noticeably weakened in the spectra of P(OEGMA)$_x$-*b*-P(CAT)$_y$-NC samples. This potentially indicates successful interaction of catechol block with the NC surface.

The crystal structure of bare and P(OEGMA)$_x$-*b*-P(CAT)$_y$-NC samples was evaluated by XRD analysis. The XRD pattern of bare NC (Fig. 3a) shows the major crystallite planes of the pure cubic fluorite structure of NC in accordance with the reference card (JCDD PDF 034-0394) at 2Theta angles of 28.59°, 33.18°, 47.57°, 56.43°, 59.18°, 69.46°, 76.81°, 79.18°, and 88.40° corresponding to (111), (200), (220), (311), (222), (400), (331), (420), and (422) planes, respectively. The obtained selected area electron diffraction (SAED) image for bare NC (Fig. 3b) also exhibits the Debye–Scherrer diffraction rings in agreement with the observed planes in the XRD pattern. No peak broadening and/or peak shift was observed for P(OEGMA)$_x$-*b*-P(CAT)$_y$-NC samples, indicating that copolymer coating of NC did not affect its crystallinity.

XPS analysis was carried out to understand whether coating NC with P(OEGMA)$_x$-*b*-P(CAT)$_y$ resulted in the reduction of Ce^{4+} to Ce^{3+} and therefore an increase in Ce^{3+}/Ce^{4+} ratio which could affect NC antioxidant performance. Fig. 4 illustrates the acquired Ce3d spectra for bare and P(OEGMA)$_x$-*b*-P(CAT)$_y$-NC samples. Deconvolution using the Thermo Avantage v5.9931 program enabled the calculation of the Ce^{3+}/Ce^{4+} ratio for each sample (Table 1).[42] Evidently, and in accordance with the blue-shifts observed in the UV-Vis spectra (Fig. 2d), the calculated Ce^{3+}/Ce^{4+} ratio for P(OEGMA)$_{25}$-*b*-P(CAT)$_7$-NC, P(OEGMA)$_{55}$-*b*-P(CAT)$_4$-NC, and P(OEGMA)$_{55}$-*b*-P(CAT)$_7$-NC showed an increase of 118%, 57%, and 82% respectively, relative to that of bare NC. Also, since each oxygen vacancy corresponds to two Ce^{3+} in principle[43] (as the release of each oxygen atom leaves two electrons which then reduce two Ce^{4+} (ref. 44)), the concentration of oxygen vacancies ($[V_O^{\cdot\cdot}]$) could be calculated based on $\frac{1}{2}[Ce^{3+}]$ for each sample.[45] As can be seen in Table 1, coating NC with P(OEGMA)$_{25}$-*b*-P(CAT)$_7$, P(OEGMA)$_{55}$-*b*-P(CAT)$_4$, and P(OEGMA)$_{55}$-*b*-P(CAT)$_7$ led to an increase of around 7.9%, 4.2%, and 5.9% in $[V_O^{\cdot\cdot}]$, respectively. The relatively lower Ce^{3+}/Ce^{4+} ratio and $[V_O^{\cdot\cdot}]$ of P(OEGMA)$_{55}$-*b*-P(CAT)$_4$-NC compared to P(OEGMA)$_{25}$-*b*-P(CAT)$_7$-NC and P(OEGMA)$_{55}$-*b*-P(CAT)$_7$-NC may arise from its lower number of CAT units that were assumed to be responsible for the reduction of Ce^{4+} to Ce^{3+}. Additionally, given the general XPS survey results (Fig. S21†), a noticeable increase in concentration of C and N was observed for P(OEGMA)$_x$-*b*-P(CAT)$_y$-NC samples with respect to bare NC (Table 1), further attesting to the successful addition of the copolymer coating to the surface of NC.

In order to understand the weight percentage of the P(OEGMA)$_x$-*b*-P(CAT)$_y$ coating on the surface of NC, and enable calculation of the grafting density, TGA was conducted on freeze-dried samples. As illustrated in Fig. 5a, bare NC exhibited minimal weight loss of around 0.5% in the range of 85–200 °C, likely associated with evaporation of residual water, and further a small weight loss of around 0.8% in the range of 200–400 °C, potentially related to adsorbed impurities. Overall, bare NC was stable against temperature increase up to 1000 °C. In contrast, notable weight loss of 12.01% (at 200–418 °C), 9.20% (at 200–430 °C), and 11.65% (at 200–435 °C) was observed for P(OEGMA)$_{25}$-*b*-P(CAT)$_7$-NC, P(OEGMA)$_{55}$-*b*-P(CAT)$_4$-NC, and P(OEGMA)$_{55}$-*b*-P(CAT)$_7$-NC, respectively. This likely arises from decomposition of the corresponding copolymer layer on the surface of NC. The slightly higher surface coating achieved by P(OEGMA)$_{25}$-*b*-P(CAT)$_7$ and P(OEGMA)$_{55}$-*b*-P(CAT)$_7$ may be due to their higher number of anchoring units in comparison with P(OEGMA)$_{55}$-*b*-P(CAT)$_4$. Using

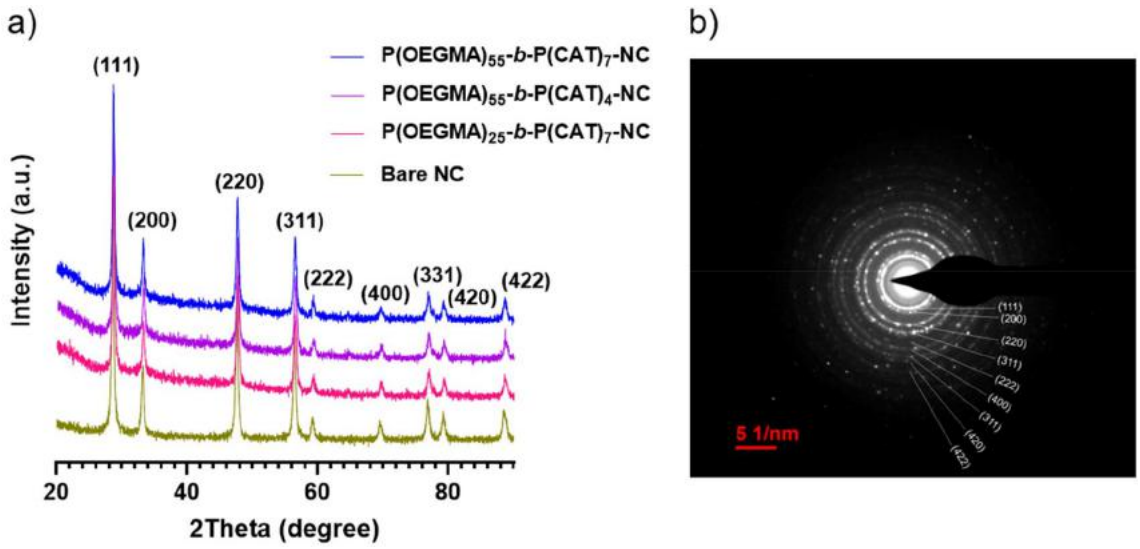

Fig. 3 (a) XRD patterns of the bare and P(OEGMA)$_x$-*b*-P(CAT)$_y$-NC samples exhibiting the main crystallite planes of NC (JCDD PDF 034–0394). (b) Selected area electron diffraction (SAED) image of bare NC illustrating the crystallite planes in accordance with the 2Theta angles observed in the corresponding XRD pattern.

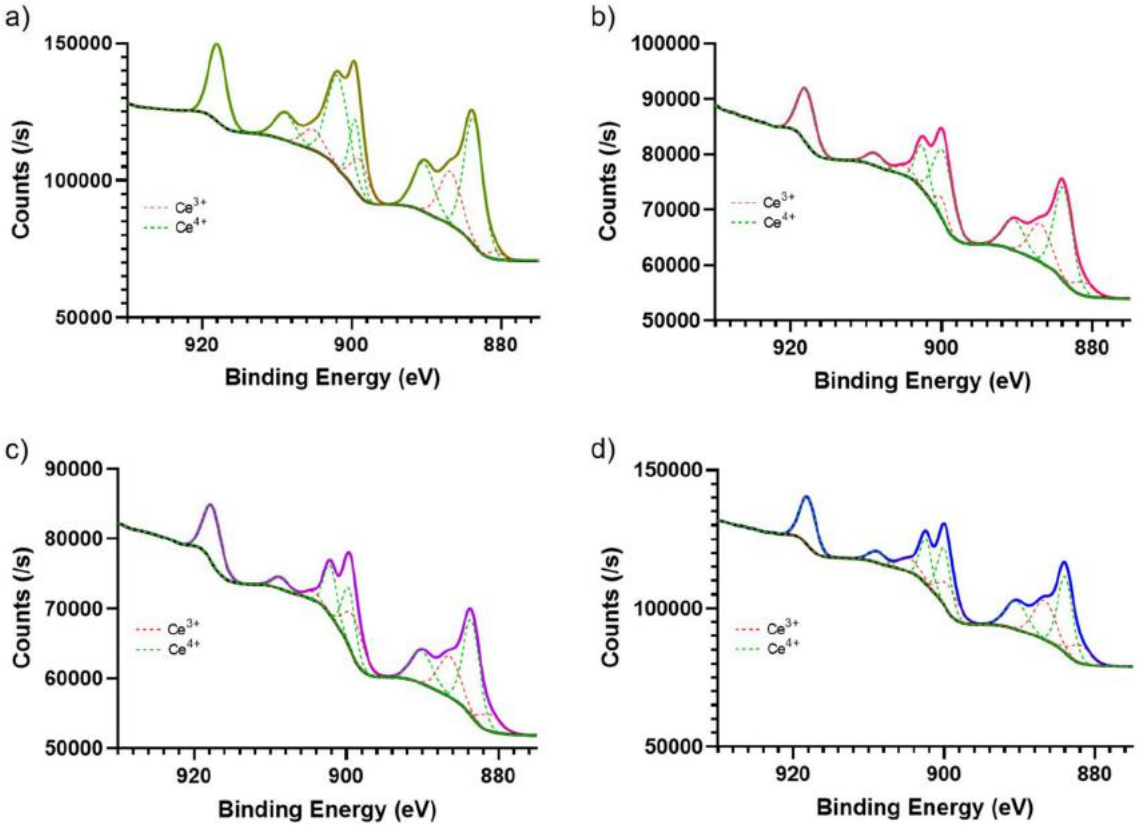

Fig. 4 XPS Ce3d spectra for (a) bare NC, (b) P(OEGMA)$_{25}$-*b*-P(CAT)$_7$-NC, (c) P(OEGMA)$_{55}$-*b*-P(CAT)$_4$-NC, and (d) P(OEGMA)$_{55}$-*b*-P(CAT)$_7$-NC illustrating the main peaks along with the deconvoluted Ce^{3+} and Ce^{4+} peaks.

Table 1 The calculated Ce^{3+}/Ce^{4+} ratios and Ce^{4+} concentration for bare and P(OEGMA)$_x$-*b*-P(CAT)$_y$-NC samples based on the corresponding deconvoluted Ce3d spectra, as well as the relative concentrations (%) of the main elements of the P(OEGMA)$_x$-*b*-P(CAT)$_y$ layer, C and N, calculated based on the obtained total XPS surveys (Fig. S21†). $[V_O^{\cdot\cdot}]$ is concentration of the oxygen vacancies calculated based on $\frac{1}{2}[Ce^{3+}]$

	Ce^{3+}/Ce^{4+}	Ce^{4+} (%)	C (%)	N (%)	$[V_O^{\cdot\cdot}]$ (%)
Bare NC	0.28	77.81	11.84	0.04	11.09
P(OEGMA)$_{25}$-*b*-P(CAT)$_7$-NC	0.61	61.94	31.72	1.97	19.03
P(OEGMA)$_{55}$-*b*-P(CAT)$_4$-NC	0.44	69.34	33.35	1.20	15.33
P(OEGMA)$_{55}$-*b*-P(CAT)$_7$-NC	0.51	66.09	35.73	1.59	16.95

formula (1) according to TGA results, grafting densities of 0.172, 0.068, and 0.087 (chains per nm^2) were calculated for P(OEGMA)$_{25}$-*b*-P(CAT)$_7$-NC, P(OEGMA)$_{55}$-*b*-P(CAT)$_4$-NC, and P(OEGMA)$_{55}$-*b*-P(CAT)$_7$-NC, respectively (Fig. 5b). Thus, the grafting density of P(OEGMA)$_{55}$-*b*-P(CAT)$_7$-NC was about 22% higher than that of P(OEGMA)$_{55}$-*b*-P(CAT)$_4$-NC. On the other hand, the grafting density of P(OEGMA)$_{25}$-*b*-P(CAT)$_7$-NC was almost two-fold greater than that of the other samples, most likely due to the shorter block length of P(OEGMA) in P(OEGMA)$_{25}$-*b*-P(CAT)$_7$. The shorter hydrophilic block length could mitigate steric hinderance and thus allow more copolymer chains to access the NC surface. Since P(OEGMA)$_x$-*b*-P(CAT)$_y$ copolymers have a non-linear structure, and the core NC exhibited irregularities in shape, it was not possible to accurately calculate the brush height for each sample. Nevertheless, based on the derived eqn (2) (*vide supra*), the height ratio of P(OEGMA)$_{25}$-*b*-P(CAT)$_7$-NC to P(OEGMA)$_{55}$-*b*-P(CAT)$_4$-NC and P(OEGMA)$_{55}$-*b*-P(CAT)$_7$-NC was calculated to be 0.79 and 0.75, respectively, suggesting a more stretched structure for the latter two coated materials. It is also worth noting that the significant difference in zeta potential for P(OEGMA)$_{55}$-*b*-P(CAT)$_7$-NC and P(OEGMA)$_{55}$-*b*-P(CAT)$_4$-NC, along with their comparable grafting densities, further substantiates the contribution of unattached/free catechol units to the observed residual negative surface charges.

3.3. Colloidal stability analysis for bare NC and P(OEGMA)$_x$-*b*-P(CAT)$_y$-NC

As a complementary approach to the Derjaguin–Landau–Verwey–Overbeek (DLVO) theory, Gambinossi *et al.*[46] presented the below model to explain the role of the major elements contributing to colloidal stability/instability:

$$\phi(h) = \phi_{\mathrm{vdW}}(h) + \phi_{\mathrm{electrostatic}}(h) + \phi_{\mathrm{hydration}}(h) + \phi_{\mathrm{osmotic}}(h) \quad (3)$$

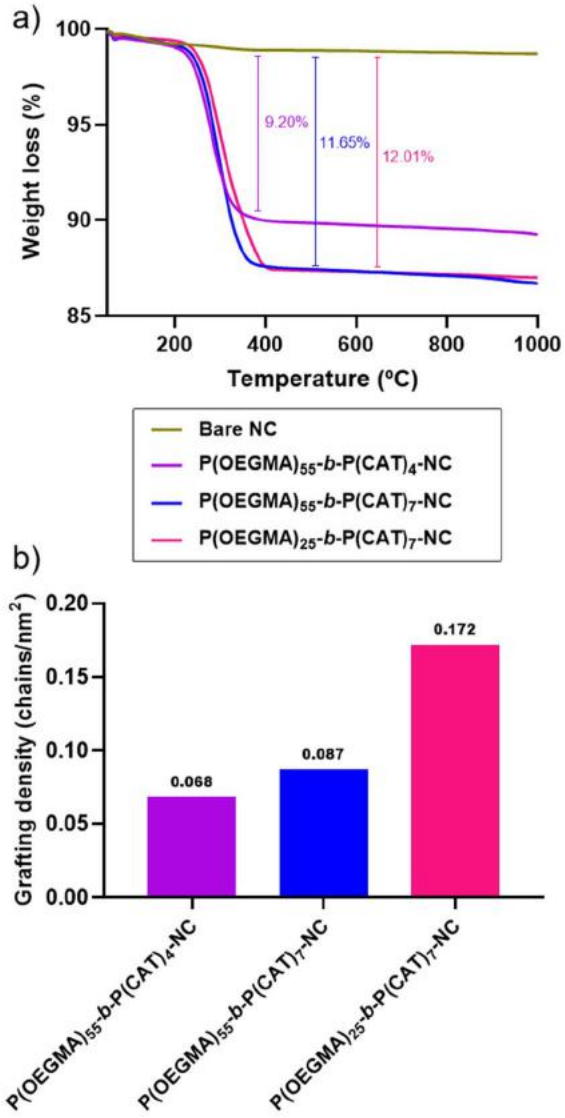

Fig. 5 (a) TGA thermograms demonstrating the determined weight loss percentage in response to an increase in temperature for bare and P(OEGMA)$_x$-*b*-P(CAT)$_y$-NC samples. (b) Grafting density values for P(OEGMA)$_x$-*b*-P(CAT)$_y$-NC samples calculated based on the corresponding weight loss percentages.

where $\phi(h)$ is the total potential energy of interaction, *i.e.*, the sum of attractive van der Waals $\phi_{\mathrm{vdW}}(h)$, repulsive electrostatic $\phi_{\mathrm{electrostatic}}(h)$, hydration $\phi_{\mathrm{hydration}}(h)$, and osmotic $\phi_{\mathrm{osmotic}}(h)$ forces. Of note, since the electrostatic and osmotic components of this model are interconnected, they can be combined into a single term to provide a clearer picture of the contributing forces.[47] Within this context, the aims of the present work were to (1) decrease the |zeta potential| value in order to curb the salt/counter ion effect and (2) provide a relatively thick hydrophilic coating on the surface of NC that could increase the hydration force, and the steric repulsion between the nanoparticles. Here, UV-Vis spectrophotometry was applied to study colloidal stability. As previously reported by Nandani Rai and S. Kanagaraj,[23] colloidal instability stems from aggregation, which results in precipitation based on Stokes' drag equation $\left(v_s = \frac{2}{9}\frac{\Delta\rho g r}{\eta}\right)$, where v_s is the sedimentation velocity, $\Delta\rho$ is the difference in density between the particles and medium, g is the gravitational constant, r is the radius of particles, and η is the dynamic viscosity of the dispersant. Additionally, absorbance is related with concentration according to the Beer–Lambert law: ($A = \varepsilon bC$), where A is absorbance, ε is the molar absorptivity, b is the path length, and C concentration.[48] Thus, since aggregation leads to precipitation of nanoparticles and therefore a decrease in their concentration in the supernatant, UV-Vis spectrophotometry is able to provide insights into the colloidal stability of bare and P(OEGMA)$_x$-*b*-P(CAT)$_y$-NC samples in PBS medium.

The stability of P(OEGMA)$_{25}$-*b*-P(CAT)$_7$-NC, possessing the shortest hydrophilic block, was comparable to that of bare NC up to 6 h, and showed around 9% improvement in long term stability (*i.e.*, 24 h and 48 h) (Fig. 6 and S22†). Increasing the length of the hydrophilic block (*i.e.*, using P(OEGMA)$_{55}$ instead of P(OEGMA)$_{25}$) improved steric repulsion and hydration forces, with P(OEGMA)$_{55}$-*b*-P(CAT)$_7$-NC showing around 9% improvement in stability up to 6 h, increasing to around 18.5% when assessed over longer period of time (*i.e.*, 24 h and 48 h). Additionally, the increased brush dimensions calculated for P(OEGMA)$_{55}$-*b*-P(CAT)$_7$-NC could have led to a thicker coating layer and thus a lower swelling ratio for P(OEGMA)$_{55}$-*b*-P(CAT)$_7$ with respect to P(OEGMA)$_{25}$-*b*-P(CAT)$_7$. It is also worth noting that since their determined zeta potential values were comparable, the salt effect could be considered equivalent for both systems.

Examination of the catechol block length also revealed insightful results. Specifically, as compared to bare NC, P(OEGMA)$_{55}$-*b*-P(CAT)$_4$-NC showed around 20% improvement in stability up to 6 h which increased to *ca.* 24.5% in long term (*i.e.*, 24 h and 48 h). In comparison to P(OEGMA)$_{55}$-*b*-P(CAT)$_7$-NC, which possessed the same hydrophilic block length, P(OEGMA)$_{55}$-*b*-P(CAT)$_4$-NC exhibited higher stability, likely stemming from its close-to-neutral zeta potential (−3.7 mV), which would decrease the impact of salt effects on colloidal stability. To scrutinise the significance of the obtained results, the experiment was repeated for P(OEGMA)$_{55}$-*b*-P(CAT)$_4$-NC, as the best performing system, and compared to bare NC (Fig. S23†). As a result, P(OEGMA)$_{55}$-*b*-P(CAT)$_4$-NC exhibited a significantly lower precipitation ($P < 0.05$) at the 2, 4, 6, and 24 h time intervals relative to that of the bare NC.

In addition to decreasing absorbance of NC over time, incremental plasmon peak broadening was also observed (Fig. S22a–c†). To characterise this, the full width at half-maximum (FWHM) value of each spectrum was calculated *via* non-linear curve fitting using the Gaussian function on OriginPro 9.1, and the plasmon peak broadening index (PPBI) was determined as $\mathrm{PPBI}(\%) = \frac{\mathrm{FWHM}_t}{\mathrm{FWHM}_0} \times 100$, where FWHM_t and FWHM_0 were calculated at time "t" and time zero. The calculated PPBI values (Fig. 6b) provided insights into the poly-

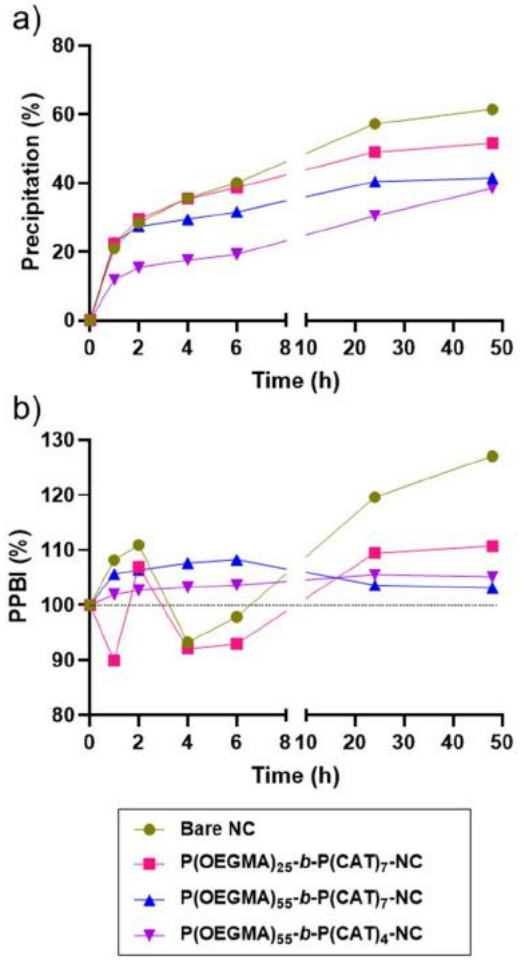

Fig. 6 Colloidal stability analysis for bare and P(OEGMA)$_x$-*b*-P(CAT)$_y$-NC samples in PBS (1x, pH 7.4) medium at NC concentration of 100 μg mL^{-1} at room temperature: (a) the calculated precipitation percentages over 48 h based on the corresponding UV-Vis absorbance values at wavelength ranges of 300–316 nm, 293–300 nm, 299–302 nm, and 298–302 nm for bare NC, P(OEGMA)$_{25}$-*b*-P(CAT)$_7$-NC, P(OEGMA)$_{55}$-*b*-P(CAT)$_4$-NC, and P(OEGMA)$_{55}$-*b*-P(CAT)$_7$-NC, respectively. (b) Plasmon peak broadening index (PPBI) values, indicating polydispersity trends, over 48 h determined based on the full width at half maximum (FWHM) values of the corresponding UV-Vis spectra calculated *via* a non-linear curve fitting by the Gaussian function on OriginPro 9.1.

dispersity of nanoparticles over time.[49–52] Hence, the average 8.6% and 12.6% fluctuations (relative to the baseline PPBI = 100%) demonstrated by P(OEGMA)$_{25}$-*b*-P(CAT)$_7$-NC and bare NC, respectively, could indicate their lower colloidal stability as compared to P(OEGMA)$_{55}$-*b*-P(CAT)$_7$-NC and P(OEGMA)$_{55}$-*b*-P(CAT)$_4$-NC, with average fluctuations of 5.7% and 3.6%, respectively. One tentative explanation for these results might be that dynamic interactions between the nanoparticles (*i.e.*, repulsive and attractive forces) could give rise to transient formation and disintegration of aggregates or agglomerates that may be reflected in polydispersity changes over time.

Further, a blue-shift was observed for each spectrum over time. To explain this, the band-gap energy was calculated for every time interval *via* extrapolation of the Tauc equation: $(\alpha h\nu)^2 = A(h\nu - E_g)$, where α is the absorption coefficient, h is Planck's constant = 6.6260×10^{-34} J s, ν is the frequency (Hz), A is the energy independent constant, and E_g is the band-gap energy (eV). The overall increase in band-gap energy for each sample (Fig. S22e†) was largely in accordance with the observed blue-shift in their corresponding UV-Vis spectra (Fig. S22a–c†), suggesting a decrease in size of the nanoparticles in the supernatant due to the electron confinement effect.[53] It is worth noting that P(OEGMA)$_{55}$-*b*-P(CAT)$_7$-NC and P(OEGMA)$_{55}$-*b*-P(CAT)$_4$-NC showed a smaller blue-shift compared to bare NC and P(OEGMA)$_{25}$-*b*-P(CAT)$_7$-NC, which might be due to their superior colloidal stability.

Taken together, the applied methodology based on UV-Vis spectrophotometry provided insightful information regarding the amount of precipitated nanoparticles over time (demonstrated by the decrease in absorbance) and, at the same time, their dynamic interactions/movements in the supernatant (based on the corresponding PPBI and bang-gap energy values).

3.4. Investigation of antioxidant activity

In order to investigate the interplay between colloidal stability and antioxidant activity for NC, CAT- and SOD-like activity analyses were performed for bare and P(OEGMA)$_x$-*b*-P(CAT)$_y$-NC samples.

3.4.1. CAT-like activity. CAT-like activity was analysed using an established method,[25] wherein the reaction of terephthalic acid (TA) with OH$^\bullet$ radicals generated due to decomposition of H_2O_2 in PBS (1×, pH 7.4), results in formation of 2-hydroxyterephthalic acid which has a broad fluorescent peak centred at around 425 nm. Hence, elimination of H_2O_2 by bare and P(OEGMA)$_x$-*b*-P(CAT)$_y$-NC samples is expected to decrease the intensity of the 2-hydroxyterephthalic acid peak and provide an indication of CAT-like activity. Importantly, since the duration of the analysis was 6 h, the colloidal stability results obtained at 6 h (Fig. 6a) are relevant for the following discussion.

The obtained results indicate that bare NC, P(OEGMA)$_{25}$-*b*-P(CAT)$_7$-NC, P(OEGMA)$_{55}$-*b*-P(CAT)$_7$-NC, and P(OEGMA)$_{55}$-*b*-P(CAT)$_4$-NC exhibited noticeable H_2O_2 elimination activities of 40.9, 38.6, 45.0, 57.7%, respectively (Fig. 7a and b). However, there was no statistically significant difference between the measured CAT-like activity of bare NC and that of P(OEGMA)$_x$-*b*-P(CAT)$_y$-NC samples. Indeed, polymer coated NC maintained their CAT-like activity at a level comparable to that of bare NC, despite the relatively higher colloidal stability of the former. A collection of factors are likely to account for these results, including the impact of P(OEGMA)$_x$-*b*-P(CAT)$_y$ coating layer on impeding the interaction of H_2O_2 with the surface of NC, as well as the lower concentration of Ce^{4+} in P(OEGMA)$_x$-*b*-P(CAT)$_y$-NC samples (Table 1).[11] It is worth mentioning that the relatively higher $[V_O^{\cdot\cdot}]$ of P(OEGMA)$_x$-*b*-P(CAT)$_y$-NC samples with respect to bare NC (Table 1) did not lead to a significant increase in their CAT-like activity, while Celardo *et al.* previously highlighted the role of oxygen vacancies in facilitating the antioxidant activity of NC by providing active sites required

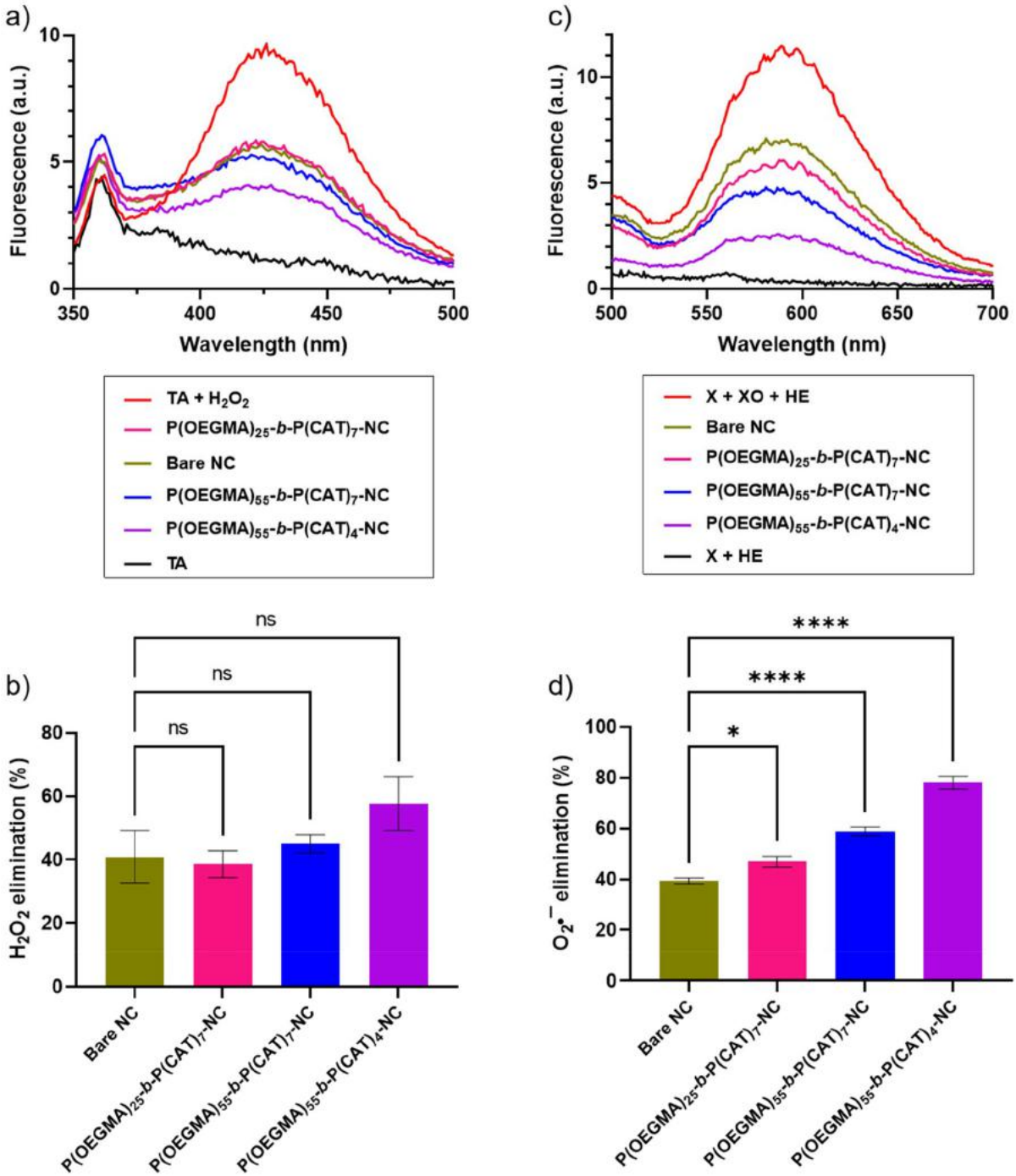

Fig. 7 Antioxidant activity analysis for bare and P(OEGMA)$_x$-*b*-P(CAT)$_y$-NC: (a) the obtained fluorescence spectra for CAT-like activity analysis exhibiting a broad emission peak at around 425 nm due to 2-hydroxyterephthalic acid, the fluorescent product of the reaction between terephthalic acid (TA) and H_2O_2 in PBS (1×, pH 7.4) medium in the absence and presence of the nanozyme samples. (b) The calculated H_2O_2 elimination capacity (*i.e.*, CAT-like activity) for each nanozyme sample based on the corresponding fluorescence intensities as compared to those of the positive (TA + H_2O_2) and negative (TA) controls. (c) The obtained fluorescence spectra for SOD-like activity analysis showing a broad emission peak at around 590 nm due to the oxidation of hydroethidine (HE) by the $O_2^{\bullet-}$ radicals, generated from the reaction of xanthine (X) and xanthine oxidase (XO), in PBS (10×, pH 7.4) medium in the absence and presence of the nanozyme samples. (d) The calculated $O_2^{\bullet-}$ elimination performance (*i.e.*, SOD-like activity) for each nanozyme sample based on the corresponding fluorescence intensities relative to those of the positive (X + XO + HE) and negative (X + HE) controls. The results are reported as mean ± SEM values (n = 4). Statistical significance was calculated *via* ordinary one-way ANOVA with Dunnett's multiple comparisons *post hoc* test (GraphPad Prism 9.0.1) with a 95% confidence interval. ns: no significant, * $P \leq 0.05$, **** $P \leq 0.0001$.

for interaction with $O_2^{\bullet-}$ and H_2O_2 molecules.[54] Importantly, the results also mean that the catechol anchoring units did not adversely affect the interaction of H_2O_2 with Ce ions at the surface of NC. In contrast, Baldim *et al.* reported that phosphonic ligands, with strong affinity towards Ce ions, hindered efficient adsorption and decomposition of H_2O_2 at the surface of PEG coated NC.[16]

3.4.2. SOD-like activity. To interrogate the capacity of bare and P(OEGMA)$_x$-*b*-P(CAT)$_y$-NC samples to neutralise $O_2^{\bullet-}$ radicals, the SOD-like activity was analysed using the hydroethidine (HE) probe method.[26] In this method HE is oxidised by the $O_2^{\bullet-}$ radicals generated through the reaction of xanthine (X) and xanthine oxidase (XO) in PBS (10×, pH 7.4) medium, with the resulting product exhibiting a broad fluorescent peak at around 600 nm. Attenuation of this signal upon application of bare and P(OEGMA)$_x$-*b*-P(CAT)$_y$-NC samples indicates their potential SOD-like function (Fig. 7c).

As illustrated in Fig. 7d, bare NC eliminated about 40% of the generated $O_2^{\bullet-}$ radicals, while P(OEGMA)$_{25}$-*b*-P(CAT)$_7$-NC, P(OEGMA)$_{55}$-*b*-P(CAT)$_7$-NC, and P(OEGMA)$_{55}$-*b*-P(CAT)$_4$-NC $O_2^{\bullet-}$ eliminated 47%, 59%, and 78%, respectively. The observed improvement in SOD-like activity for P(OEGMA)$_x$-*b*-P(CAT)$_y$-NC samples is consistent with previous studies which indicate that the SOD-like function of NC is dependent on Ce^{3+} concentration.[11,16] As discussed before, XPS measurements (Table 1) revealed a noticeable increase in Ce^{3+}/Ce^{4+} ratios for all P(OEGMA)$_x$-*b*-P(CAT)$_y$-NC samples. In addition, it can be inferred that the catechol anchoring units did not hamper interaction of $O_2^{\bullet-}$ with oxygen vacancy sites at the surface of P(OEGMA)$_x$-*b*-P(CAT)$_y$-NC. Delving further into differences between the coated samples, P(OEGMA)$_{55}$-*b*-P(CAT)$_7$-NC demonstrated a higher SOD-like activity compared to P(OEGMA)$_{25}$-*b*-P(CAT)$_7$-NC, which correlates with the higher colloidal stability and almost 2-fold lower grafting density of the former. Interestingly, the Ce^{3+}/Ce^{4+} of P(OEGMA)$_{55}$-*b*-P(CAT)$_7$-NC was lower than that of P(OEGMA)$_{25}$-*b*-P(CAT)$_7$-NC (0.51 *vs.* 0.61), indicating the relative importance of colloidal stability and grafting density on the observed SOD-like activity. P(OEGMA)$_{55}$-*b*-P(CAT)$_4$-NC exhibited a noticeable improvement in $O_2^{\bullet-}$ elimination capacity with respect to the other two P(OEGMA)$_x$-*b*-P(CAT)$_y$-NC samples, leading us to investigate the colloidal stability of bare and P(OEGMA)$_{55}$-*b*-P(CAT)$_4$ coated NC samples under assay conditions (PBS (10×, pH 7.4), 100 μg mL^{-1} NC, 10 min). Specifically, this study was performed to investigate the effect of salt concentration (1× *vs.* 10×) on colloidal stability of these samples. In PBS 10× solution bare NC exhibited around 19% precipitation after 10 min, in contrast to only 5% for P(OEGMA)$_{55}$-*b*-P(CAT)$_4$-NC (Fig. S24a–c†). It is worth noting that bare NC had shown about 21% precipitation in PBS 1× after 1 h (Fig. 6a), indicating the substantial effect of salt concentration on colloidal stability as discussed previously. Also, the peak broadening index (PPBI) of bare NC demonstrated an average deviation of around 15% from the 100% baseline as compared to around 4% for P(OEGMA)$_{55}$-*b*-P(CAT)$_4$-NC which further supports the improved colloidal stability of P(OEGMA)$_{55}$-*b*-P(CAT)$_4$-NC relative to bare NC. As noted above, the improved stability likely results from the significantly lower |zeta potential| of P(OEGMA)$_{55}$-*b*-P(CAT)$_4$-NC, counteracting the adverse salt/counter ion effects.

Overall, considering the totality of CAT- and SOD-like activity results, it is clear that an interplay between a number of factors, including colloidal stability, grafting density of copolymers, Ce^{3+}/Ce^{4+} ratio, $[V_O^{\bullet\bullet}]$, and the anchoring block's interactions with the NC surface, dictate the antioxidant activity of an NC-based nanozyme.

3.5. Cytotoxicity assay

To assess the *in vitro* tolerability of P(OEGMA)$_x$-*b*-P(CAT)$_y$-NC samples, a cytotoxicity assay was performed *via* the Alamar Blue method against HEK293 cells at a constant NC concentration of 100 μg mL^{-1}, as used for the CAT- and SOD-like activity assays. As illustrated in Fig. S25,† both bare and P(OEGMA)$_x$-*b*-P(CAT)$_y$-NC samples showed no appreciable cytotoxicity toward normal cells compared to the negative control. Indeed, biocompatibility of P(OEGMA) based polymers and NC based nanozymes has already been described in several studies.[31,32,38,55–57] These results provide a strong basis for more extensive investigation of the *in vitro* antioxidant activity for P(OEGMA)$_x$-*b*-P(CAT)$_y$-NC in future studies.

4. Conclusions

To probe the nexus between colloidal stability and antioxidant activity of NC, the present study reported the synthesis of a library of three copolymeric stabilising agents (*i.e.*, P(OEGMA)$_{25}$-*b*-P(CAT)$_7$, P(OEGMA)$_{55}$-*b*-P(CAT)$_4$, and P(OEGMA)$_{55}$-*b*-P(CAT)$_7$), and their subsequent grafting to the surface of bare NC *via* the catechol functionalities of the (CAT) block. P(OEGMA)$_x$-*b*-P(CAT)$_y$-NC showed a decrease in |zeta potential| values as compared to bare NC, likely due to the neutrally charged P(OEGMA) blocks, while the unattached/free catechol units contributed to the obtained negative zeta potential values. XPS results revealed an increase in Ce^{3+}/Ce^{4+} ratios for P(OEGMA)$_x$-*b*-P(CAT)$_y$-NC due to the reduction of Ce^{4+} ions by the catechol functionalities of the (CAT) block. The determined grafting densities for P(OEGMA)$_{55}$-*b*-P(CAT)$_4$-NC and P(OEGMA)$_{55}$-*b*-P(CAT)$_7$-NC were around 2-fold lower than that of P(OEGMA)$_{25}$-*b*-P(CAT)$_7$-NC, as the latter had a shorter P(OEGMA) block that could minimise the potential effect of steric hinderance. Regarding the nexus between colloidal stability and antioxidant activity, P(OEGMA)$_{55}$-*b*-P(CAT)$_4$-NC gave rise to the starkest trends. Specifically, in comparison with bare NC, P(OEGMA)$_{55}$-*b*-P(CAT)$_4$-NC exhibited an enhanced colloidal stability in PBS medium (1×, pH 7.4) over the both short-term (up to 21%, 6 h) and long-term (up to 23%, 48 h). This could be ascribed to its relatively neutral surface charge (zeta potential −3.7 eV) and the repulsive steric and hydration forces provided by the long P(OEGMA)$_{55}$ block. Further, while bare NC (zeta potential −32 eV) showed 19% precipitation in PBS medium (10×, pH 7.4) after just 10 min, P(OEGMA)$_{55}$-*b*-P

$(CAT)_4$-NC exhibited only 5% precipitation under the same conditions, highlighting the important role of counter ions in determining the colloidal stability of charged nanomaterials. $P(OEGMA)_{55}$-*b*-$P(CAT)_4$-NC also demonstrated higher CAT- and SOD-like activities (*i.e.*, increases of 41% ($P > 0.05$) and 78% ($P < 0.0001$), respectively), as compared to those of bare NC. These results indicate that an interplay between several factors, including improved colloidal stability, increased Ce^{3+}/Ce^{4+} ratio, and relatively lower grafting density contribute to the antioxidant activity of $P(OEGMA)_x$-*b*-$P(CAT)_y$-NC, and the use of catechol anchoring units does not interfere with the interactions between $O_2^{\bullet-}$ or H_2O_2 and the active sites on the NC surface. Overall, these results demonstrate the potential utility of catechol-containing polymers for the preparation of surface-engineered NC with preserved (and even enhanced) antioxidant performance.

Data availability

The data supporting this article have been included as part of the ESI† and are also available from the corresponding author upon reasonable request.

Conflicts of interest

The authors declare no conflict of interest.

Acknowledgements

The authors acknowledge use of facilities within the Monash X-ray Platform to carry out XPS analysis. The authors also wish to acknowledge financial support from Monash University.

References

1 M. Ghorbani, H. Derakhshankhah, S. Jafari, S. Salatin, M. Dehghanian, M. Falahati and A. Ansari, *Nano Today*, 2019, **29**, 100775.
2 M. Ghorbani, Z. Izadi, S. Jafari, E. Casals, F. Rezaei, A. Aliabadi, A. Moore, A. Ansari, V. Puntes and M. Jaymand, *Nanomedicine*, 2021, **16**, 1133–1151.
3 L. Ma, J.-J. Zheng, N. Zhou, R. Zhang, L. Fang, Y. Yang, X. Gao, C. Chen, X. Yan and K. Fan, *Nat. Commun.*, 2024, **15**, 233.
4 B. C. Nelson, M. E. Johnson, M. L. Walker, K. R. Riley and C. M. Sims, *Antioxidants*, 2016, **5**, 15.
5 M. S. Lord, J. F. Berret, S. Singh, A. Vinu and A. S. Karakoti, *Small*, 2021, **17**, 2102342.
6 C. Korsvik, S. Patil, S. Seal and W. T. Self, *Chem. Commun.*, 2007, 1056–1058.
7 E. Saito and B. H. Bielski, *J. Am. Chem. Soc.*, 1961, **83**, 4467–4468.
8 A. Filippi, F. Liu, J. Wilson, S. Lelieveld, K. Korschelt, T. Wang, Y. Wang, T. Reich, U. Pöschl and W. Tremel, *RSC Adv.*, 2019, **9**, 11077–11081.
9 J. M. Dowding, T. Dosani, A. Kumar, S. Seal and W. T. Self, *Chem. Commun.*, 2012, **48**, 4896–4898.
10 N. J. Lawrence, J. R. Brewer, L. Wang, T.-S. Wu, J. Wells-Kingsbury, M. M. Ihrig, G. Wang, Y.-L. Soo, W.-N. Mei and C. L. Cheung, *Nano Lett.*, 2011, **11**, 2666–2671.
11 I. Celardo, J. Z. Pedersen, E. Traversa and L. Ghibelli, *Nanoscale*, 2011, **3**, 1411–1420.
12 T. Pirmohamed, J. M. Dowding, S. Singh, B. Wasserman, E. Heckert, A. S. Karakoti, J. E. King, S. Seal and W. T. Self, *Chem. Commun.*, 2010, **46**, 2736–2738.
13 S. Das, J. M. Dowding, K. E. Klump, J. F. McGinnis, W. Self and S. Seal, *Nanomedicine*, 2013, **8**, 1483–1508.
14 T. L. Moore, L. Rodriguez-Lorenzo, V. Hirsch, S. Balog, D. Urban, C. Jud, B. Rothen-Rutishauser, M. Lattuada and A. Petri-Fink, *Chem. Soc. Rev.*, 2015, **44**, 6287–6305.
15 J. Schubert and M. Chanana, *Curr. Med. Chem.*, 2018, **25**, 4553–4586.
16 V. Baldim, N. Yadav, N. Bia, A. Graillot, C. Loubat, S. Singh, A. S. Karakoti and J.-F. Berret, *ACS Appl. Mater. Interfaces*, 2020, **12**, 42056–42066.
17 H. J. Kwon, M. Y. Cha, D. Kim, D. K. Kim, M. Soh, K. Shin, T. Hyeon and I. Mook-Jung, *ACS Nano*, 2016, **10**, 2860–2870.
18 R. N. Mitra, R. Gao, M. Zheng, M. J. Wu, M. A. Voinov, A. I. Smirnov, T. I. Smirnova, K. Wang, S. Chavala and Z. Han, *ACS Nano*, 2017, **11**, 4669–4685.
19 F. Ercole, C.-J. Kim, N. V. Dao, W. K. L. Tse, M. R. Whittaker, F. Caruso and J. F. Quinn, *Biomacromolecules*, 2023, **24**, 387–399.
20 C. Chevigny, D. Gigmes, D. Bertin, J. Jestin and F. Boué, *Soft Matter*, 2009, **5**, 3741–3753.
21 J. Li, B. Hu, K. Yang, B. Zhao and J. S. Moore, *ACS Macro Lett.*, 2016, **5**, 819–822.
22 C. M. Wijmans and E. B. Zhulina, *Macromolecules*, 1993, **26**, 7214–7224.
23 N. Rai and S. Kanagaraj, *ACS Omega*, 2022, **7**, 22363–22376.
24 S. Tsunekawa, T. Fukuda and A. Kasuya, *J. Appl. Phys.*, 2000, **87**, 1318–1321.
25 C. Hao, A. Qu, L. Xu, M. Sun, H. Zhang, C. Xu and H. Kuang, *J. Am. Chem. Soc.*, 2019, **141**, 1091–1099.
26 Y. Liu, Y. Zhang, Q. Liu, Q. Wang, A. Lin, J. Luo, Y. Du, Y.-W. Lin and H. Wei, *Analyst*, 2021, **146**, 1872–1879.
27 X. Ju, A. Fučíková, B. Šmíd, J. Nováková, I. Matolínová, V. Matolín, M. Janata, T. Bělinová and M. Hubálek Kalbáčová, *RSC Adv.*, 2020, **10**, 39373–39384.
28 F. Caputo, M. Mameli, A. Sienkiewicz, S. Licoccia, F. Stellacci, L. Ghibelli and E. Traversa, *Sci. Rep.*, 2017, **7**, 4636.
29 I. A. T. Moleavin, A. Fifere, A. L. Lungoci, I. Rosca, A. Coroaba, D. Peptanariu, V. Nastasa, S. A. Pasca, A. C. Bostanaru, M. Mares and M. Pinteala, *Nanomaterials*, 2019, **9**, 1565.
30 S. Sakib, F. Bakhshandeh, S. Saha, L. Soleymani and I. Zhitomirsky, *Sol. RRL*, 2021, **5**, 2100512.

31 M. Liu, J.-C. Leroux and M. A. Gauthier, *Prog. Polym. Sci.*, 2015, **48**, 111–121.
32 J. F. Lutz, *J. Polym. Sci., Part A: Polym. Chem.*, 2008, **46**, 3459–3470.
33 C.-J. Kim, F. Ercole, E. Goudeli, S. K. Bhangu, J. Chen, M. Faria, J. F. Quinn and F. Caruso, *Chem. Mater.*, 2022, **34**, 7468–7480.
34 P. C. Chrostowski, A. M. Dietrich and I. H. Suffet, *Water Res.*, 1983, **17**, 1627–1633.
35 M. A. Macchione, C. Biglione and M. Strumia, *Polymers*, 2018, **10**, 527.
36 K. J. Mitchell, K. A. Abboud and G. Christou, *Nat. Commun.*, 2017, **8**, 1–7.
37 S. Nimesh, in *Gene Therapy*, ed. S. Nimesh, Woodhead Publishing, 2013, pp. 43–63, DOI: 10.1533/9781908818645.43.
38 S. Yang, J. Ji, M. Luo, H. Li and Z. Gao, *Nanoscale*, 2021, **13**, 16349–16361.
39 S. V. Sokolov, K. Tschulik, C. Batchelor-McAuley, K. Jurkschat and R. G. Compton, *Anal. Chem.*, 2015, **87**, 10033–10039.
40 W.-J. Jeon, H. Kim and S.-H. Byeon, *Colloids Surf., A*, 2022, **640**, 128416.
41 H. Li, Z. Wang, Q. Song, M. Guo, Z. Jiao, Y. Wang, Y. Liu, Y. Zhu and P. Zhang, *Mater. Des.*, 2023, **225**, 111426.
42 E. Bêche, P. Charvin, D. Perarnau, S. Abanades and G. Flamant, *Surf. Interface Anal.*, 2008, **40**, 264–267.
43 R. Mehmood, S. S. Mofarah, W.-F. Chen, P. Koshy and C. C. Sorrell, *Inorg. Chem.*, 2019, **58**, 6016–6027.
44 P. Dutta, S. Pal, M. S. Seehra, Y. Shi, E. M. Eyring and R. D. Ernst, *Chem. Mater.*, 2006, **18**, 5144–5146.
45 W. F. Chen, C. M. D. S. Malacco, R. Mehmood, K. K. Johnson, J. L. Yang, C. C. Sorrell and P. Koshy, *Mater. Sci. Eng., C*, 2021, **120**, 111663.
46 F. Gambinossi, S. E. Mylon and J. K. Ferri, *Adv. Colloid Interface Sci.*, 2015, **222**, 332–349.
47 H. J. Butt, K. Graf and M. Kappl, *Physics and Chemistry of Interfaces*, Wiley, 2013.
48 S. Zhang, L. Li and A. Kumar, *Materials Characterization Techniques*, CRC Press, 2008.
49 R. D. Averitt, S. L. Westcott and N. J. Halas, *J. Opt. Soc. Am. B*, 1999, **16**, 1824–1832.
50 J. Lim, A. Eggeman, F. Lanni, R. D. Tilton and S. A. Majetich, *Adv. Mater.*, 2008, **20**, 1721–1726.
51 S. Sangar, S. Sharma, V. K. Vats, S. Mehta and K. Singh, *J. Cleaner Prod.*, 2019, **228**, 294–302.
52 S. Agnihotri, S. Mukherji and S. Mukherji, *RSC Adv.*, 2014, **4**, 3974–3983.
53 M. Singh, M. Goyal and K. Devlal, *J. Taibah Univ. Sci.*, 2018, **12**, 470–475.
54 I. Celardo, M. De Nicola, C. Mandoli, J. Z. Pedersen, E. Traversa and L. Ghibelli, *ACS Nano*, 2011, **5**, 4537–4549.
55 Y. Cao, K. Cheng, M. Yang, Z. Deng, Y. Ma, X. Yan, Y. Zhang, Z. Jia, J. Wang, K. Tu, J. Liang and M. Zhang, *J. Nanobiotechnol.*, 2023, **21**, 21.
56 R. G. Daré, E. Kolanthai, C. J. Neal, Y. Fu, S. Seal, C. V. Nakamura and S. O. S. Lautenschlager, *Antioxidants*, 2023, **12**, 190.
57 M. A. Davoodbasha, K. Saravanakumar, A. M. Abdulkader, S. Y. Lee and J. W. Kim, *ACS Appl. Bio Mater.*, 2019, **2**, 1792–1801.